TECHNISCHE UNIVERSITÄT WIEN

MEDIZINISCHE UNIVERSITÄT WIEN

DIPLOMARBEIT

Selective Photoreceptor Stimulation via Silent Substitution for Rod and Cone Specific pRF Mapping

zur Erlangung des akademischen Grades

Diplom-Ingenieurin

im Rahmen des Studiums

066 453 Biomedical Engineering

eingereicht von

Johanna Maria Bogner, BSc

Martrikelnummer 01425435

ausgeführt am Atominstitut
der Fakultät für Technische Physik der Technischen Universität Wien
in Zusammenarbeit mit dem Zentrum für Medizinische Physik und Biomedizinische Technik der Medizinischen Universität Wien

Betreuung:
Ao.Univ.Prof.in Dipl.-Ing.in Dr.in techn. Christina Streli
Mitwirkung:
David Linhardt, PhD
Assoc.-Prof. Priv.-Doz. DI Dr. Christian Windischberger
Ass.Prof.in Dipl.-Ing.in Dr.in techn. Karin Poljanc

Wien, 13.05.2025 _____ _____

(Unterschrift Verfasserin) (Unterschrift Betreuerin)

Danksagung

Zuerst möchte ich Prof. Christina Streli herzlich danken - für die Betreuung dieser Arbeit und die investierte Zeit. Mein Dank gilt ebenso Prof. Karin Poljanc, die mir geholfen hat, den richtigen Ort und die passende Betreuung für meine Arbeit zu finden, und die mich in der finalen Phase meines Studiums mit Rat und Unterstützung begleitet hat.

Ich danke auch Prof. Christian Windischberger, der mir nicht nur ermöglicht hat, wertvolle praktische Erfahrungen im fMRI Bereich zu sammeln, sondern auch stets ein offenes Ohr für meine Fragen hatte. Von den ersten Ideen bis zur finalen Ausarbeitung stand er mir in Worten und Taten zur Seite.
Ein besonderer Dank gilt David Linhardt – ohne seine Unterstützung wäre diese Arbeit nicht möglich gewesen. Für all die Stunden, die er in mich und mein Projekt investiert hat, für seine geduldigen Erklärungen, seinen klugen Rat und seine hilfreichen Anregungen, die mir halfen, mich im Zuge dieser Arbeit weiterzuentwickeln.
Mein Dank gilt ebenso allen Kolleginnen und Kollegen im MR-Zentrum, für die angenehme Atmosphäre und dafür, dass ich mich von Anfang an willkommen gefühlt habe – insbesondere Florian Gisinger für seine Freundschaft und den Zusammenhalt während unserer gemeinsamen Zeit.

Ein großes Dankeschön geht auch an Sarah Stellmach – für all die Gespräche und die aufmunternden Worte in schwierigen Momenten. Diese Erfahrung mit dir teilen zu dürfen, hat vieles leichter und nicht ganz so unüberwindbar erscheinen lassen. Ebenso danke ich Jessica Roßmann, Hemma Mogy und Anna Wulz – dafür, dass ich das große Ganze nicht aus den Augen verloren habe. Für all die gemeinsamen Lernphasen und die gegenseitige Unterstützung in herausfordernden Zeiten.

Mein tief empfundener Dank gilt meiner Familie, die mir immer wieder geholfen hat, den Blick auf das Wesentliche zu richten und mir gezeigt hat, was im Leben wirklich wichtig ist.

Abschließend möchte ich mich von Herzen bei meinen Eltern bedanken. Ich bin euch unendlich dankbar dafür, dass ihr mir ermöglicht habt, meinen Träumen zu folgen und meinen eigenen Weg zu suchen. Danke, dass ihr immer an mich geglaubt und mich bedingungslos unterstützt habt.

Contents

Abstract

Blood oxygenation level dependent functional magnetic resonance imaging (BOLD fMRI) is a non-invasive technique used to study human brain activity. It exploits the different magnetic susceptibilities of oxygenated and deoxygenated hemoglobin. During image acquisition participants are shown a stimulus, the type of which, depends on the brain region of interest.

The fMRI-based technique used to investigate the retinotopic organisation of the human visual system, is called population receptive field (pRF) mapping. It allows the mapping of areas in the visual field to their corresponding regions of the primary visual cortex. Typically used stimuli include a combination of wedges and rings or bar stimuli, both revealing a high-contrast checkerboard pattern.
In typical pRF experiments both types of photoreceptors of the retina, rods and cones, are activated, due to the overlapping spectral sensitivity of the individual photoreceptors. The goal of this thesis is to perform pRF mapping, with tailored stimulus designs that favour activity in either rods or cones. To achieve this, the "silent substitution" approach was used. It is based on the fact that each photoreceptor subtype has a specific sensitivity profile across different wavelengths. By using stimuli with specifically designed colour and intensity properties, individual photoreceptor subtypes can be activated separately.

To activate rods or cones individually, two stimuli were generated. Due to the properties of the video projector, it was only possible to silence a maximum of two photoreceptor types per stimulus. The rod-selective stimulus silenced L- and M-cones and the cone-selective stimulus silenced rods. Special consideration was also taken in regards to the light conditions during the experiments. Measurements were obtained in seven healthy subjects using a 3T SIEMENS Prisma Fit scanner. For the first set of measurements, five participants were presented with the rod-selective stimulus at low and very-low luminance levels and the cone-selective stimulus at high luminance levels. As cones are hardly activated at low luminance levels and rods are saturated at high luminance levels, different light levels were used, in addition to the stimulus design, to ensure maximum response in the photoreceptor of interest. Three functional runs were recorded. At each luminance level: one run with full-field stimulation and two runs with bar-shaped stimuli. In a second study, three participants were shown the same stimuli as in the first study but the light conditions were switched. The cone-selective stimulus was shown at low and very-low luminance levels while the rod-selective stimulus was shown at full brightness. The acquired data was preprocessed and analysed to calculate visual field maps. From them, plots of the distribution of the activated voxels over eccentricity were generated.

The results show a distribution of activated voxels that matches the distribution of cones on the retina for the cone-selective and rod-selective stimulus at high luminance levels. For the rod-selective stimulus the response is due to the activation of the S-cone. For the rod-selective stimulus at low luminance levels the distribution of activated voxels matches the distribution of rods, indicating the activation of pre-

dominantly rods. This was ensured by the stimulus design in combination with the low luminance levels, that ensured no additional activation of S-cones. The cone-selective stimulus at low luminance levels also resulted in a voxel distribution that matches the distribution of rods on the retina, indicating that the stimulus could not fully silence rod photoreceptors.
In summary, it is shown in this thesis that we were able to selectively activate individual photoreceptor subtypes by combining silent substitution with measurement conditions, that were adjusted to match the properties of the photoreceptor of interest.

Zusammenfassung

Blutoxigenierungsabhängige funktionelle Magnetresonanztomographie (BOLD fMRT) ist eine nichtinvasive Methode zur Untersuchung der menschlichen Gehirnaktivität. Sie basiert auf den unterschiedlichen magnetischen Suszeptibilitäten von sauerstoffreichem und sauerstoffarmem Hämoglobin. Während der Datenaufnahme wird den Teilnehmern ein Stimulus gezeigt, die Art des Stimulus hängt dabei von der zu untersuchenden Region ab.

Eine, auf fMRT basierende, Methode zur Untersuchung der retinotopischen Organisation des menschlichen visuellen Systems nennt sich population receptive field (pRF) mapping. Sie ermöglicht die Zuordnung von Regionen des Gesichtsfeldes zu den entsprechenden Regionen des primären visuellen Kortex. Typischerweise verwendete Stimuli sind entweder eine Kombination aus Kreissegmenten und Ringen oder balkenförmige Stimuli, beide zeigen ein Schachbrettmuster mit hohem Kontrast.
In typischen pRF-Experimenten werden alle Arten von Photorezeptoren auf der Netzhaut, Stäbchen und Zapfen, aktiviert. Dies liegt daran, dass sich die Lichtspektren, bei denen die Rezeptoren angeregt werden, überlappen. Das Ziel dieser Diplomarbeit ist es pRF mapping durchzuführen, mit einem Stimulus Design, dass darauf zu geschneidert ist die Aktivität von entweder Stäbchen oder Zapfen zu begünstigen. Um dies zu erreichen, wurde der "Silent Substitution" Ansatz verwendet. Er basiert auf der Tatsache, dass jede Photorezeptor Unterart ein spezifisches Empfindlichkeitsprofil für verschiedene Wellenlängen aufweist. Durch die Verwendung von Stimului mit speziell gewählten Farb- und Intensitätseigenschaften können individuelle Photorezeptor Unterarten einzeln angeregt werden.

Um Stäbchen oder Zapfen einzeln anzuregen, wurde zwei Stimuli erzeugt. Aufgrund der Eigenschaften des Videoprojektors, war es nur möglich maximal zwei Arten von Photorezeptoren stillzulegen. Beim stäbchen-selektiven Stimulus wurden L- und M-Zapfen stillgelegt und beim zapfen-selektiven Stimulus wurden Zapfen stillgelegt. Besonderes Augenmerk wurde auch auf die Lichtverhältnisse während der Messung gelegt. Die Messungen wurden mit einem 3T SIEMENS Prisma Fit Scanner an sieben gesunden Probanden durchgeführt. Im Zuge der ersten Messungen wurde fünf Teilnehmern der stäbchen-selektive Stimulus bei niedrigen und sehr niedrigen Lichtverhältnissen und der zapfen-selektive Stimulus bei hellen Lichtverhältnissen präsentiert. Da Zapfen bei niedrigen Lichtverhältnissen kaum angeregt werden

und Stäbchen bei hellen Lichtverhältnissen gesättigt sind, wurden unterschiedliche Lichtverhältnisse verwendet um, zusätzlich zum Design der Stimuli, die maximale Reaktion des gewollten Photorezeptors sicherzustellen. Drei funktionale Messungen wurden durchgeführt. Pro Helligkeitslevel: ein Durchgang mit einem Stimulus, der das gesamte Gesichtsfeld stimuliert und zwei Durchgänge mit einem balkenförmigen Stimulus. Im Zuge einer zweiten Studie wurde drei Teilnehmern die gleichen Stimuli gezeigt, aber mit umgekehrten Lichtverhältnissen. Der zapfen-selektive Stimulus wurde bei schwachen und sehr schwachen Lichtverhältnissen präsentiert und der stäbchen-selektive bei hellen Lichtverhältnissen. Die erfassten Daten wurden verarbeitet und analysiert um Aktivitätskarten vom visuellen Kortex zu berechnen. Diese wurde verwendet um Grafiken der Verteilung der aktiven Voxel über die Exzentrizität zu erstellen.

Die Ergebnisse zeigen, dass, für den zapfen-selektiven und den stäbchen-selektiven Stimulus bei voller Helligkeit, die Verteilung der aktiven Voxel mit der Verteilung der Zapfen auf der Retina übereinstimmt. Im Falle des stäbchen-selektiven Stimulus kommt die Aktivität durch die Aktivierung der S-cones zustande. Für den stäbchen-selektiven Stimulus bei schwachen Lichtverhältnissen stimmt die Verteilung der aktiven Voxel mit der Verteilung der Stäbchen überein, was auf die Aktivierung von vorwiegend Stäbchen hindeutet. Der zapfen-selektive Stimulus bei schwachen Lichtverhältnissen resultierte auch in einer Verteilung der Voxel, die mit der Verteilung der Stäbchen übereinstimmt. Das deutet darauf hin, dass dieser Stimulus Stäbchen nicht vollständig stilllegen konnte.
Zusammenfassend wird diese Diplomarbeit zeigen, dass wir in der Lage waren individuelle Photorezeptoren Unterarten selektiv anzuregen, indem wir Silent Substitution mit Messbedingungen kombiniert haben, die auf die Eigenschaften des betreffenden Photorezeptors angepasst wurden,

1 Introduction

Magnetic resonance imaging (MRI) is based on the works of Lauterbur [53] and Mansfield [60], who introduced the use of field gradients in the 1970s. Their work in turn is based on the studies on nuclear magnetic resonance (NMR) by Bloch [6] and Purcell [68] in the 1940s, where they were able to measure the NMR signal from a water and a paraffin sample.

A particular branch of MRI is functional magnetic resonance imaging (fMRI), which is used to assess brain activity. The mechanism of fMRI depends on changes in blood flow during neural activity which was already hypothesised in the end of the 19$^{\text{th}}$ century by Roy and Sherrington [71]. Modern blood oxygen level dependent (BOLD) fMRI was introduced by Owaga et al. in 1990 [64]. It is a non-invasive imaging method used to study neuronal activity. BOLD fMRI is based on the differences in magnetic susceptibility of oxygenated and deoxygenated hemoglobin. Oxygen shields the iron atom in the centre of hemoglobin, which reduces field distortions and signal loss [16]. Since neuronal activation leads to an increase in oxygenated blood, the measured signal is increased compared to a non active state [36].

fMRI is being used to study many different regions of the brain. The region of interest for this work is the visual cortex, particularly its retinotopic organization. The latter refers to describing the property that adjacent areas in the visual field are mapped on adjacent areas on the visual cortex. Areas in the centre of the visual field are mapped on the posterior region of the visual cortex and the further the region lies in the periphery of the visual field, the further anterior are the corresponding regions of the visual cortex. This retinotopic organization is studied using a special analysis method on fMRI data, referred to as retinotopic mapping [83]. The state-of-the-art tool for assessing retinotopic mapping is called population receptive field (pRF) mapping. This method models the response of every voxel as a two-dimensional Gaussian function on the visual field. The so-called receptive field is connected to the corresponding areas of the visual field. To achieve this, functional images are acquired while participants are viewing specific stimulus shapes. Within this thesis a bar stimulus based on the work of Dumoulin and Wandell in 2008 [28] was used.

As a result of the overlapping spectral sensitivities of the different photoreceptor types and because black and white stimuli are used, pRF mapping generally maps the input of all photoreceptors. The interest of this thesis lies on the specific activation of individual photoreceptor subtypes. Therefore, the silent substitution approach was used. Silent substitution is a method that makes use of the differences in spectral sensitivities of photoreceptor subtypes. It was first used by Ishihara in 1906 [47] and then further established by Donner and Rushton in 1959 [27]. It can be used to calculate a chromatic pair that activates one photoreceptor, while keeping the activation of others constant [75]. For our study, two stimuli were generated, one selectively activating rods and one cones.

This thesis begins with an overview on the physical background of interest. The physical basics of NMR, MRI and fMRI are explained in chapters 2.1 to 2.3. Here

the principle of spins, the framework of the imaging process as well as the physiological basis of fMRI are introduced. Chapter 2.4 presents information on the human visual system, with focus on the retina, the visual pathway and the visual cortex. The way information is processed at different stages of the visual system is of special interest as well. Retinotopic mapping is introduced in chapter 2.5. The main focus of this chapter is the concept of retinotopic organization and pRF mapping. Chapter 2.6 closes the background segment with providing information on silent substitution.

In chapter 3, the steps that were taken to design the stimulus are explained. Chapter 4 provides context on the experimental conditions as well as the analysis methods. Two different stimuli were used to perform measurements on seven healthy subjects on a 3T scanner. In addition to the different stimuli themselves, the luminance conditions during the measurements were changed as well. In Study 1, five participants were presented with the rod-selective stimulus at low and very-low luminance levels and the cones-selective stimulus at high luminance levels. In Study 2, three healthy subjects were presented with the same stimuli but the light conditions were switched. The rod-selective stimulus was shown at high luminance and the cone-selective stimulus was shown at low and very-low luminance levels. The different light conditions influence the activation of the photoreceptors. Rods are only activated at very low luminance levels, as they become saturated at bright light. Cones on the other hand are only active at high luminance levels, because they are insensitive to low-light conditions. The acquired data was used to generate cortex maps of the regions of activation as well as plots showing the distribution of activated voxels per degree of eccentricity of the visual field. The results are presented in chapter 5 and discussed in chapter 6. It will be shown that we were able to selectively activate individual photoreceptor subtypes by using a combination of silent substitution and light conditions, that were adjusted to match the properties of the selected receptor.

2 Background

2.1 Nuclear Magnetic Resonance

In 1946 Bloch [6] and Purcell [68] independently extended the early concepts of nuclear magnetic resonance (NMR), which were based on the work of Rabi [69] in the 1938. They were able to measure the NMR signal from a water and a paraffin sample respectively. Based on their work, Lauterbur [53] and Mansfield [60] introduced nuclear magnetic resonance imaging in 1973 [14]. Today, magnetic resonance imaging (MRI) is a powerful and non-invasive imaging modality used in clinical settings for diagnostics and research.

Physical Principles

To understand nuclear magnetic resonance (NMR) it is important to know the structure of atoms. Atoms consist of a nucleus and orbiting electrons. The nucleus is composed of protons, which possess positive charge and neutrons which are chargeless. The nucleus is surrounded by orbitals, where negatively charged electrons are located. Elements can be categorized using their atomic mass number A and their atomic number Z. The atomic number refers to the number of protons in the nucleus. The mass number is the sum of the number of protons and neutrons. If atoms have the same atomic number but different atomic mass numbers, they are called isotopes [20]. A fundamental property of the nucleus is the intrinsic spin angular momentum, $\vec{S}$. The spin can take on only discrete values, depending on the atomic number and atomic mass number [8].
In the following text, I use the classical vector model to describe magnetic resonance (MR) principles. Even though these are quantum mechanical phenomena, the classical model is a great tool to explain the macroscopic features of spins. The nuclear magnetism is represented by the nuclear magnetic moment $\vec{\mu}$ given by [55]:

$$\vec{\mu} = \gamma \vec{S} \tag{1}$$

with γ being the gyromagnetic ratio. In order to define the magnetic moment we need its magnitude as well as its orientation. The magnitude is given by:

$$\mu = \gamma \hbar \sqrt{I(I+1)} \tag{2}$$

with $\hbar$ being the Planck's constant h divided by 2π and I being the spin quantum number [55]. The value of I depends on the atomic number and mass number of a nucleus. If A and Z are even, then the spin is zero. These types of nuclei do not interact with an external magnetic field. For nuclei with an odd atomic number and even atomic mass number, I has an integer value. And if the atomic mass number and the atomic number are odd, I has a half-integer value [20].
Without an external magnetic field present, the direction of $\vec{\mu}$ is completely random [55]. The individual spin vectors of the spin system are oriented randomly in all directions and cancel each other out, when averaged over the ensemble. Therefore, no net magnetization can be observed [8]. In order to obtain macroscopic magnetization, an external magnetic field ($\vec{B_0}$) is applied. The external magnetic field is directed along the z-direction of the laboratory frame and is given by [55]:

$$\vec{B_0} = B_0 \vec{k} \tag{3}$$

The orientation of the magnetic moment $\vec{\mu}$ inherits the quantum mechanical property of assuming only discrete values, as I is discrete. While the transverse component μ_{xy} of the magnetic moment is random, the z-component is given by [55]:

$$\mu_z = \gamma m_I \hbar \tag{4}$$

with m_I being the magnetic quantum number. m_I can take a set of distinct values. For a nucleus with non-zero spin these values are given by [55]:

$$m_I = -I, -I+1, ..., I \tag{5}$$

Therefore, μ_z has (2I + 1) possible orientations with respect to the orientation of the external field. For a spin-$\frac{1}{2}$ system, with $I = \frac{1}{2}$, m_I has two possible values, $\pm\frac{1}{2}$ [55]. This is of special interest, as the ^1H nucleus has a spin of $\frac{1}{2}$. ^1H is the most frequent isotope of hydrogen, an element which is prevalent in biological tissue, and therefore, produces a strong MR signal. As a result of the two possible values for m_I, the z-component can be oriented parallel or anti-parallel to the external magnetic field $\vec{B_0}$ [20]. In MR, $\vec{B_0}$ is always assumed to be oriented along the z-direction ("up").
From a quantum-mechanical perspective the interaction between the spin and the external magnetic field is called the Zeeman splitting. This interaction results in an energy difference ΔE between the two orientations, proportional to B_0 [8]. With [55]:

- parallel:

$$E_\uparrow = -\frac{1}{2}\gamma\hbar B_0 \tag{6}$$

- anti-parallel:

$$E_\downarrow = \frac{1}{2}\gamma\hbar B_0 \tag{7}$$

This shows that the spin-down state is the higher-energy and spin-up the lower-energy state. And that the energy difference is given by $\Delta E = \gamma\hbar B_0$. Related to the difference in energy is the spin population difference. The Boltzmann relationship gives us [55]:

$$\frac{N_\uparrow}{N_\downarrow} = exp(\frac{\Delta E}{KT_s}) \tag{8}$$

with $N_\uparrow$ and $N_\downarrow$ being the number of parallel and anti-parallel spins, T_s being the absolute temperature of the spin system and K being the Boltzmann constant. By approximation this gives us [55]:

$$N_\uparrow - N_\downarrow \approx N_s \frac{\gamma\hbar B_0}{2KT_s} \tag{9}$$

Which indicates that slightly more spins are in the lower-energy state and therefore, oriented in the direction of the magnetic field [55]. This orientation of the magnetic moments results in a macroscopic magnetization $\vec{M}$. $\vec{M}$ is the vector sum of the individual magnetic moments and is oriented in the direction of the external field.

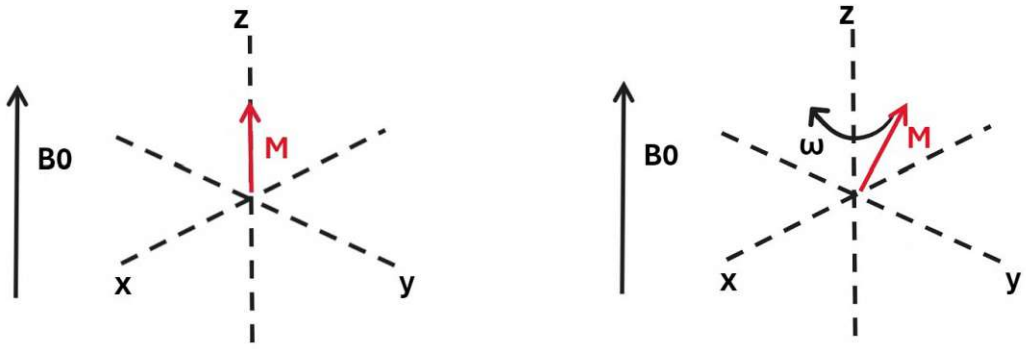

Figure 1: **Behaviour of net magnetization $\vec{M}$ in an external field $\vec{B}_0$**
$\vec{M}$ is static when parallel with the external magnetic field $\vec{B}_0$ (a). If they are not aligned, $\vec{M}$ precesses about $\vec{B}_0$ with the angular frequency ω (b) [62].

The interaction between the magnetic field and the macroscopic magnetization is given by [62]:

$$\frac{d\vec{M}}{dt} = -\gamma\vec{M} \times \vec{B} = -\vec{M} \times \vec{\omega} \tag{10}$$

Equation (10) is called the Bloch equation without relaxation.

If the magnetization and the magnetic field are parallel, the vector product $\gamma\vec{M} \times \vec{B}_0$ is zero and $\vec{M}$ is static (Figure 1a). If they are not aligned, the magnetization precesses about the direction of the magnetic field with an angular frequency ω (Figure 1b) [62].

The frequency with which the spins precess depends on the strength of $\vec{B}_0$ and is given by the Larmor equation [20]:

$$\omega_0 = \gamma B_0 \tag{11}$$

with ω_0 being the Larmor frequency [20].

The Larmor frequency corresponds to the resonance frequency of the spin system and depends linearly on the strength of the magnetic field B_0 and the gyromagnetic ratio γ, as shown in Equation (11). The different resonance frequencies for different nuclei allow the selective imaging of a specific nucleus. But in practice, the resonance frequency of a spin system may vary even if it consists of the same type of nucleus. This is mainly due to (1) inhomogeneities in the external field and (2) the chemical shift effect. If B_0 is not homogeneous, spins have different resonance frequencies at different spatial locations. The chemical shift is a result of the molecular environment of the nucleus. Electrons orbiting the nucleus produce their own weak magnetic fields, that "shields" the nucleus [55]. The degree of the shielding varies depending on the local environment, resulting in slightly different Larmor frequencies. This variation in the magnetic field is given by [15]:

$$B_{shifted}(j) = (1 - \sigma_j)B_0 \tag{12}$$

with σ_j being the shielding constant for the chemical compound j. Therefore, hydrogen nuclei (^{1}H) in water have a different Larmor frequency than those in fat [15].

Resonance Frequency Excitation

It is only possible to detect the macroscopic magnetization if $\vec{M}$ is not static. When $\vec{M}$ precesses around the external magnetic field $\vec{B}_0$ it induces electromotive force in a coil, proportional to $\frac{d\vec{M}}{dt}$ [62]. In order to manipulate $\vec{M}$, a short radio frequency (RF) pulse is applied. This excitation pulse consists of a range of frequencies and the protons absorb a part of the contained energy. They absorb the energy, where the frequency matches the protons Larmor frequency. Protons in the lower-energy state will be excited to the higher-energy state. As mentioned above (Equations (6) and (7)), the energy difference between the two states is given by [9]:

$$\Delta E = \hbar\omega_0 = \hbar\gamma B_0 \tag{13}$$

The energy difference is proportional to the Larmor frequency and therefore, the magnitude of the external magnetic field. The frequency at which energy can be absorbed is called the resonance frequency [9]. During an RF pulse the protons within the tissue interact with the electromagnetic waves. But, due to the higher amount of protons in the lower-energy state, a net absorption of energy takes place [21].
The magnetic field $\vec{B}_1$, generated by the RF pulse, is a magnetic field perpendicular to $\vec{B}_0$. It is typically turned on for a few milliseconds and is much weaker than the external magnetic field [55]. $\vec{B}_1$ can rotate the magnetization. In order to better describe this rotation, I will use a rotating frame of reference, rotating around a axis parallel to $\vec{B}_0$ with the Larmor frequency. This rotation of the frame compensates for the precession of the magnetization. Therefore, the magnetization behaves as if no static magnetic field were present and $\vec{B}_1$ is seen as a static vector perpendicular to $\vec{B}_0$ [62]. In the rotating frame the magnetization precesses around $\vec{B}_1$. When the field $\vec{B}_1$ is activated, the magnetization rotates into the xy-plane. This is called a 90° pulse (Figure 2).

After $\vec{B}_1$ is turned off, the tilted $\vec{M}$ precesses around $\vec{B}_0$. This precession induces voltage in a coil, which is placed perpendicular to the xy-plane resulting in the NMR signal [21]. The frequency of the signal is related to the external magnetic field, as can be seen in Equation (11) [9].

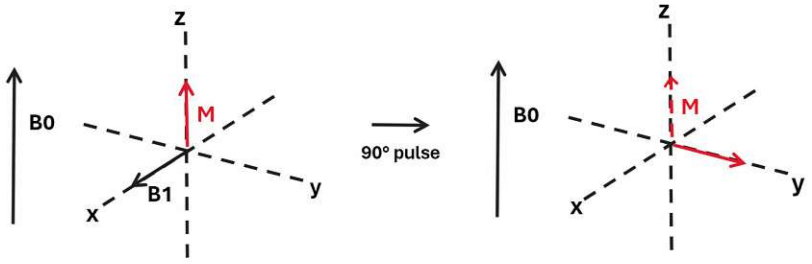

Figure 2: **90° pulse**
The 90° pulse rotates the magnetization into the transversal plane [21].

Relaxation

After rotating into the transversal plane, the magnetization $\vec{M}$ is no longer in equilibrium. When $\vec{B_1}$ is turned off, the magnetization will return to being aligned with $\vec{B_0}$. Two relaxation processes take place simultaneously: the longitudinal relaxation, which is the recovery of the longitudinal component M_z, and the transverse relaxation, which is the decay of the transverse component of the magnetization M_{xy} [55]. The processes are time-dependent and are characterized by the relaxation times T_1 and T_2 respectively [22]. Both T_1 and T_2 depend on the tissue composition as well as surroundings. For a given tissue composition T_1 is always longer than T_2 [55].

The longitudinal relaxation time T_1 is the time it takes M_z to return to 63% of its value in thermal equilibrium. This relaxation process is also called the spin-lattice relaxation, since the excited protons exchange energy with the surrounding environment ("lattice"). Directly following the 90° pulse, no longitudinal magnetization is present. With time, the protons exchange energy and the longitudinal relaxation returns (Figure 3). This is described by an exponential growth process give by [10]:

$$M_z(t) = M_0(1 - e^{-t/T_1}) \tag{14}$$

with t being the time following the RF pulse and M_0 being the value of $\vec{M}$ in equilibrium. It takes a duration of about three times T_1 for $\vec{M}$ to return to 95% of its original value [10]. As mentioned before, protons transfer their energy to their surroundings. In order for this to occur, there needs to be some type of molecular motion of the lattice. This motion has an intrinsic frequency which must match the resonance frequency of the protons, ω_0. The closer the frequencies are, the quicker the protons return to their equilibrium sate. Typically, the frequencies match better at lower resonance frequencies. And since ω_0 depends on the external magnetic field, this results in T_1 decreasing with the strength of the magnetic field [22].

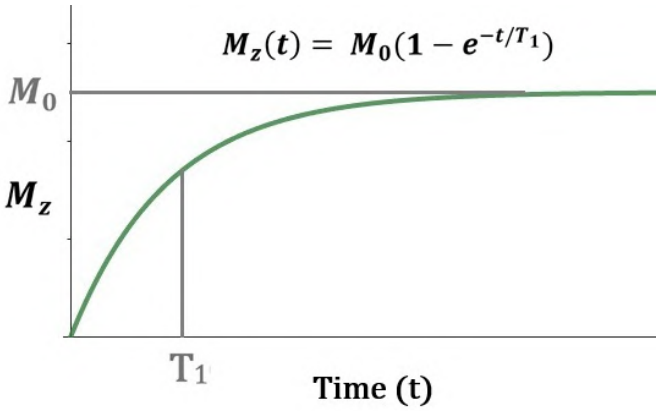

Figure 3: **Longitudinal magnetization M_z as a function of time**
Immediately after the 90° pulse no longitudinal magnetization is present. Over time, as protons transfer their energy, the magnetization returns [10].

The decay of the transverse component M_{xy} is called transverse relaxation or spin-spin relaxation. It is described by the time constant T_2 [62]. T_2 is the time it takes for M_{xy} to decay to 37% of its initial value (Figure 4). As with longitudinal relaxation, transverse relaxation follows an exponential process [10]:

$$M_{xy}(t) = M_0 e^{-t/T_2^*} \tag{15}$$

with M_0 being the transverse magnetization immediately after the 90° pulse [10].

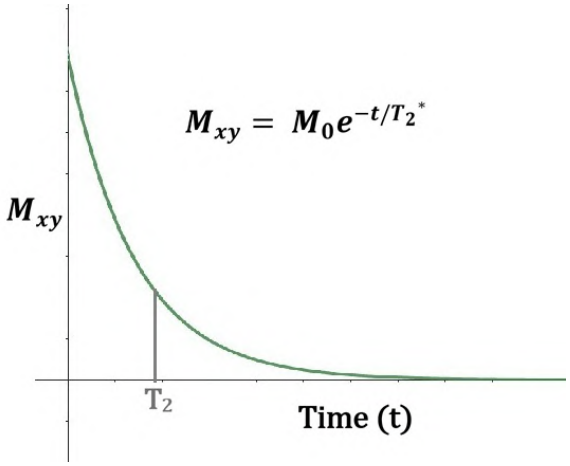

Figure 4: **Transverse magnetization M_{xy} as a function of time**
T_2 is the time it takes for the transverse magnetization M_{xy} to decay to 37% of its initial value [22].

Directly after the 90° pulse, the magnetization is flipped into the transverse plane and all spins precess at the same frequency ω_0 [10]. Over time, spins begin to fan out as they lose their phase coherence. This is due to multiple reasons. The molecular motions of adjacent spins due to rotations or vibration is one of them. Another reason is that the magnetic field that spins experience is not completely homogeneous. These changes in the local magnetic field result in ω_0 changing as

well as a loss in transverse phase coherence. The inhomogeneities in $\vec{B_0}$ are due to [22]:

- Static field inhomogeneity due to imperfections that can arise during the manufacturing of the magnet, the composition of nearby walls or other sources of metal. This field distortion is constant during the measuring time.
- Sample-induced inhomogeneity due to different magnetic susceptibilities of adjacent tissues. This inhomogeneity is caused by the sample itself and is constant as long as no movement is involved.
- Imaging gradients, where intended inhomogeneities are generated.

The different sources of field inhomogeneities mentioned above contribute to the total transverse relaxation time, $T_2{}^*$:

$$\frac{1}{T_2^*} = \frac{1}{T_2} + \frac{1}{T_{2M}} + \frac{1}{T_{2MS}} \tag{16}$$

While T_2 is the time it takes for the magnetization to decay to 37% of its initial value, T_{2M} is the relaxation time, as a result of the main field inhomogeneity and T_{2MS}, is due to the magnetic susceptibility differences [22].

Static field inhomogeneities can be compensated via so-called spin echoes. For this, a second RF pulse can be used to reverse the dephasing. Shortly after the 90° RF pulse, a 180° RF pulse is applied. The 90° pulse rotates the magnetization into the xy-plane. Some time t passes during which the spins dephase and the transverse coherence declines. Applying the 180° pulse reverses the phase of the spins, without changing their rate and direction of precession. After the time t has passed again, the protons will have regained their phase coherence (Figure 5). This method is called the spin echo sequence and results in a signal in the receiver coil called the spin echo. The time between the excitation pulse and the formation of the spin echo is called the echo time (TE) [22].

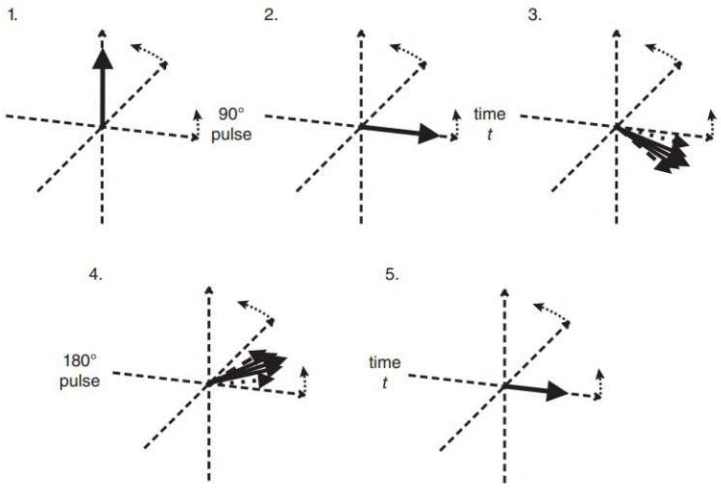

Figure 5: **Application of a 180° RF pulse following a 90° pulse** [22]
The 90° RF pules rotates the magnetization M into the transverse plane (2). During the time t dephasing of the spins takes place (3). The application of the 180 pulse reverses the phase of the spins. The spins that precessed the furthest are now behind (dashed arrow) and the slower protons are now in front (4). After the time t has passed again, the spins are aligned again (5) [10]

Bloch Equations

The magnetization $\vec{M}$ aims to return to a state of minimal energy, with $M_z = M_0$ and $M_{xy} = 0$. The Bloch equations are a set of macroscopic equations describing the time evolution of the magnetization. They include both precession and relaxation effects [14]. In the stationary frame of reference the Bloch equations are given by [4]:

$$\frac{dM_x}{dt} = \gamma(\vec{M} \times \vec{B})_x - \frac{M_x}{T_2} \tag{17a}$$

$$\frac{dM_y}{dt} = \gamma(\vec{M} \times \vec{B})_y - \frac{M_y}{T_2} \tag{17b}$$

$$\frac{dM_z}{dt} = \gamma(\vec{M} \times \vec{B})_z - \frac{M_z - M_0}{T_1} \tag{17c}$$

Equation (17c) depicts the longitudinal magnetization and the Equations (17a) and (17b) represent the transverse magnetization.

Following a 90° pulse, when $\vec{M}$ is rotated into the xy-plane, the equations simplify to [15]:

$$M_{xy} = M_0 e^{-t/T_2} \tag{18a}$$

$$M_z = M_0(1 - e^{-t/T_1}) \tag{18b}$$

2.2 Magnetic Resonance Imaging

As mentioned in Chapter 2.1, the energy a proton absorbs depends on the magnetic field strength it experiences. Magnetic resonance imaging (MRI) uses this to

spacially localize these proton frequencies [23].

Gradient fields

In MRI, linear magnetic field gradients are superimposed on the main magnetic field $\vec{B_0}$, so that the exact magnetic field depends on the location within the magnet. Typically small perturbations are applied. The resulting magnetic field is given by [23]:

$$\vec{B} = \vec{B_0} + G_T \vec{r} \vec{e_z} \tag{19}$$

with $\vec{B}$ being the magnetic field at location $\vec{r}$ and G_T being the total gradient amplitude. During a scan the gradients are applied for a short time. Three gradients are necessary for spatial encoding in three directions. In a typical sequence these gradients are referred to as slice-selection, frequency-encoding and phase-encoding gradients. These gradients are necessary to achieve spacial encoding and they must be perpendicular to each other. Gradient pulses combined with RF pulses, data sampling periods and the timing between each element are called a pulse sequence [23].

In the case of added gradients, the Larmor equation needs to be expanded to [11]:

$$\omega = \gamma(B_0 + \vec{G}\vec{r_i}) \tag{20}$$

with ω being the frequency of the proton at position $\vec{r_i}$ and $\vec{G}$ representing the gradient amplitude and direction. The resonant frequency of each proton uniquely depends on the position within the magnetic field. Therefore, the MR image is a map of these protons. The image is expressed as pixels that represent voxels (volume elements of the tissue). The pixel intensity depends on the number of protons within a voxel, weighted by T_1 or T_2 [11].

Slice Selection

The first step of the encoding process is to localize the RF excitation to a region of space. This is done by combining frequency-selective excitation with the slice-selection gradient $\vec{G_{SS}}$. The frequency-selective RF pulse consists of a central frequency (ω_i) and a narrow bandwidth of frequencies. This excitation pulse combined with the slice-selection gradient results in only narrow regions of tissue absorbing the RF energy, as only this area matches the resonance condition (Figure 6).
While the slice position is determined from the central frequency, the slice thickness Δz is determined by G_{SS}, the gradient amplitude, and $\Delta\omega_{SS}$, the bandwidth of frequencies. The thickness is changed by modifying G_{SS}, since $\Delta\omega_{SS}$ is usually fixed for a given pulse sequence. In order to achieve thinner slices, the slope of G_{SS} needs to be increased [23].

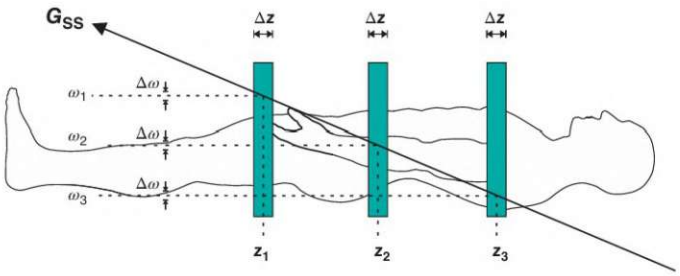

Figure 6: **Slice Selection** [23]
The slice-selective gradient $\vec{G_{SS}}$ is applied. Protons at position z_i absorb the energy of the RF pulse with the centre frequency ω_i. The protons at each position in space have a different resonance frequency [23].

Frequency Encoding

During measurements, the summed MRI signal of the whole slice is detected. During the readout the so-called readout gradient $\vec{G_{RO}}$ is applied. Following the slice-selective 90° excitation pulse, the transverse magnetization dephases, as mentioned in Chapter 2.1, and a 180° pulse leads to the formation of a spin echo. During the detection of this echo the readout gradient is applied perpendicular to the slice direction. The spins at different positions in the resulting gradient field now precess with different frequencies (Figure 7). This is reflected in the echo signal, which is measured using receiver coils and digitized for later Fourier Transformation. The corresponding positions can be determined using the magnitude of $\vec{G_{RO}}$ and the detected frequency [11].

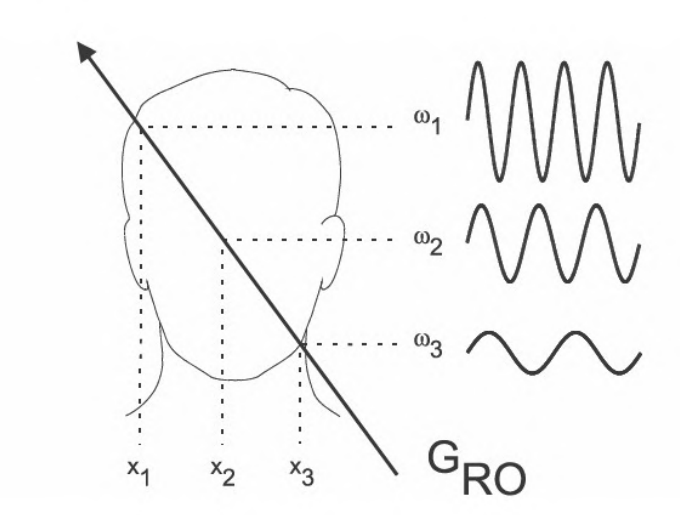

Figure 7: **Readout Gradient** [11]
After excitation with a 90° and an 180° RF pulse a spin echo is detected. During the detection, the frequency gradient $\vec{G_{RO}}$ is applied. This leads to the protons precessing with different frequencies ω_i depending on their position x_i [11].

Phase Encoding

The third gradient is the phase-encoding gradient $\vec{G_{PE}}$. It is perpendicular to both the slice-selection gradient and the readout gradient.
The spins within a slice precess at the frequency ω_0. Once the phase-encoding gradient is turned on, their precession frequency increases or decreases along the direction of the phase-encoding gradient, according to Equation (20). After $\vec{G_{PE}}$ is turned off the spins again precess at their original Larmor frequency, but now they are either ahead or behind. Therefore, a phase shift ϕ_i has been introduced, encoding for the third dimension (Figure 8). The amount of phase differences depends on the magnitude and duration of the phase-encoding gradient and the proton location [23].

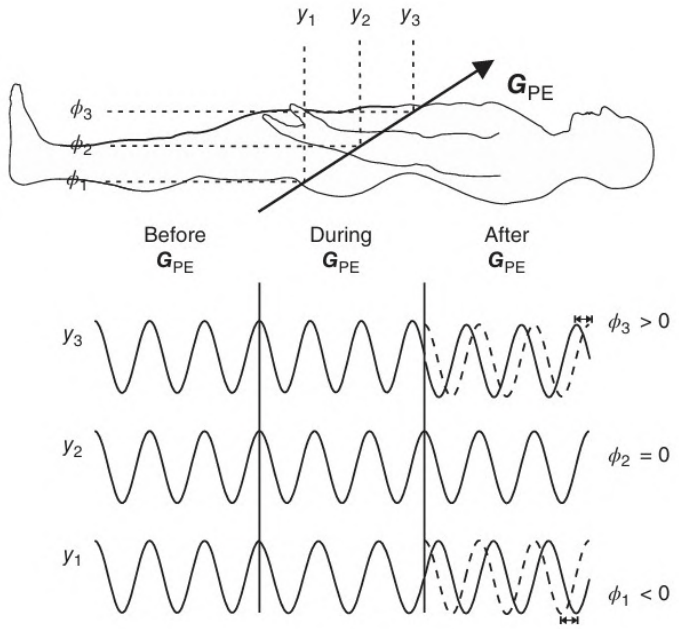

Figure 8: **Phase Encoding Gradient** [23]
Before the phase-encoding gradient $\tilde{G_{PE}}$ is applied, all spins precess at the same frequency. When the phase-encoding gradient is turned on, the precession frequency changes depending on their position y_i. The frequency increases or decreases. After $\vec{G_{PE}}$ is turned of, the spins again precess with their original Larmor frequency, but they will be either ahead or behind. This introduces a phase shift ϕ_i to the protons [23].

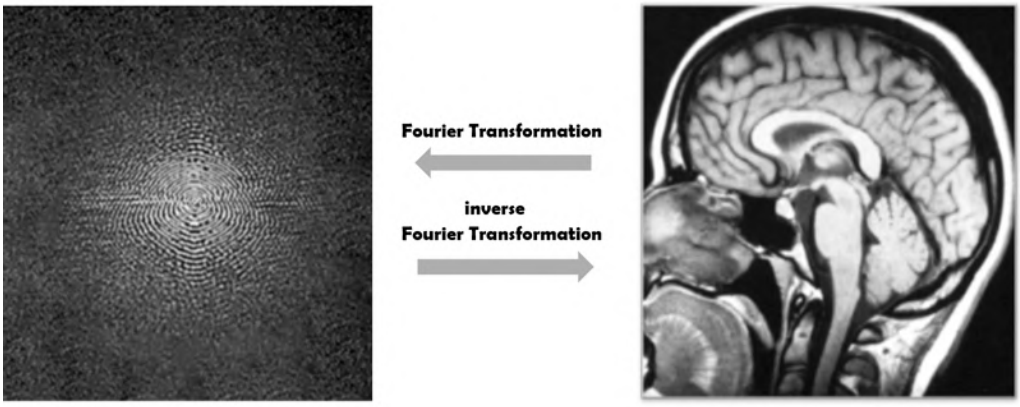

Figure 9: **Fourier Transformation between k-space and image space** Adapted from [30]

k-space

In MRI, the same data containing the information of the measured slice, exists in two spaces, the k-space and the image space. While the image data is typically used for viewing and interpretation, the k-space data represents the Fourier Transformed version of the image data (Figure 9) [12].

While the k-space contains all necessary information to reconstruct images, no point-to-point mapping exists between the two spaces. k-space consists of a grid of data points (Figure 10), where each point contributes to the transformed image in image space. Each point in k-space represents a certain spatial frequency and orientation in the image space while the value represents the amplitude of the spatial wave. The x direction corresponds to the readout direction and the y direction corresponds to different phase-encoding gradient amplitudes:

$$k_x = \gamma G_{RO} t_{RO} \tag{21}$$
$$k_y = \gamma G_{PE} t_{PE} \tag{22}$$

with t_{RO} and t_{PE} being the times for which the respective gradients are active. k-space can be navigated by using the readout and the phase-encoding gradients.

The low spatial frequency data near the centre of the k-space determines the contrast of the image and the high spatial frequency data at the periphery of the k-space determines high spatial resolution aspects, like edge definition [12]. Δk is the distance between two adjacent points and k_{max} is the distance from the centre of the k-space to the edge [31].

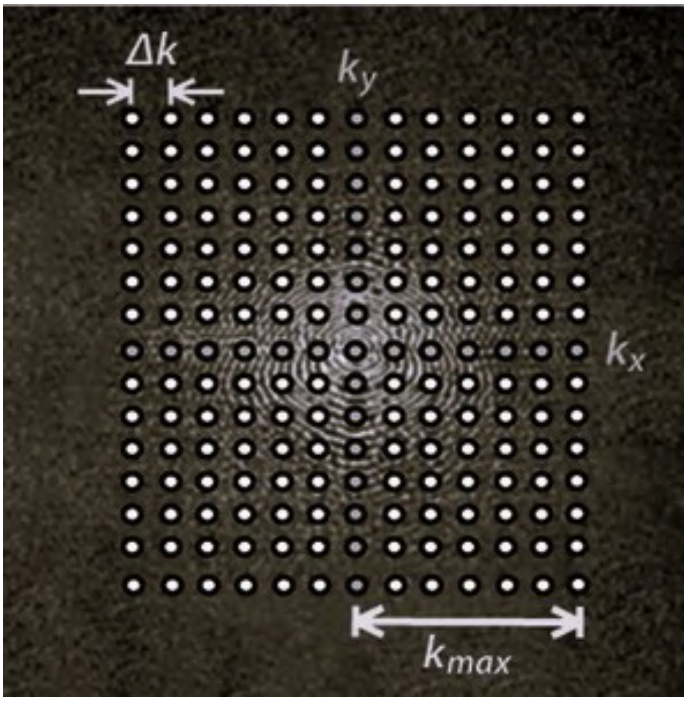

Figure 10: **The k-space grid.** Adapted from [31]

As mentioned above, the k-space data and the image data are related by Fourier Transformation. To acquire an image, prior to the Fourier Transformation, a continuos set of raw data must be acquired by sampling the echo signal throughout the k-space [24]. Fourier Transformation describes the transformation between the k-space data $S(\vec{k})$ and the image data $s(\vec{r})$ and is given by [56]:

$$s(\vec{r}) \propto \iint S(\vec{k}) e^{i\vec{k}\vec{r}} d^2k \tag{23}$$

$$S(\vec{k}) \propto \iint s(\vec{r}) e^{-i\vec{k}\vec{r}} d^2r \tag{24}$$

Equation (23) is the inverse Fourier Transform, it transforms the scanner signal $S(\vec{k})$ from the k-space to the image space.

Imaging Sequence

The order and timing of RF pulses and gradient pulses is called an imaging sequence. Sequences are described by timing diagrams, which are graphic visualizations of the different steps performed during the sequence [13].

A typical sequence is the spin echo sequence. It consists of two or more RF pulses, a 90° excitation pulse and a 180° refocusing pulse, that generates the spin echo. The repetition time TR is the time between two excitation pulses and the echo time TE is the time from the excitation pulse to the maximum of the spin echo. A timing diagram for a standard single echo sequence is shown in Figure 11. It shows the timing of the RF pulses and of the slice-selection, phase-encoding and readout

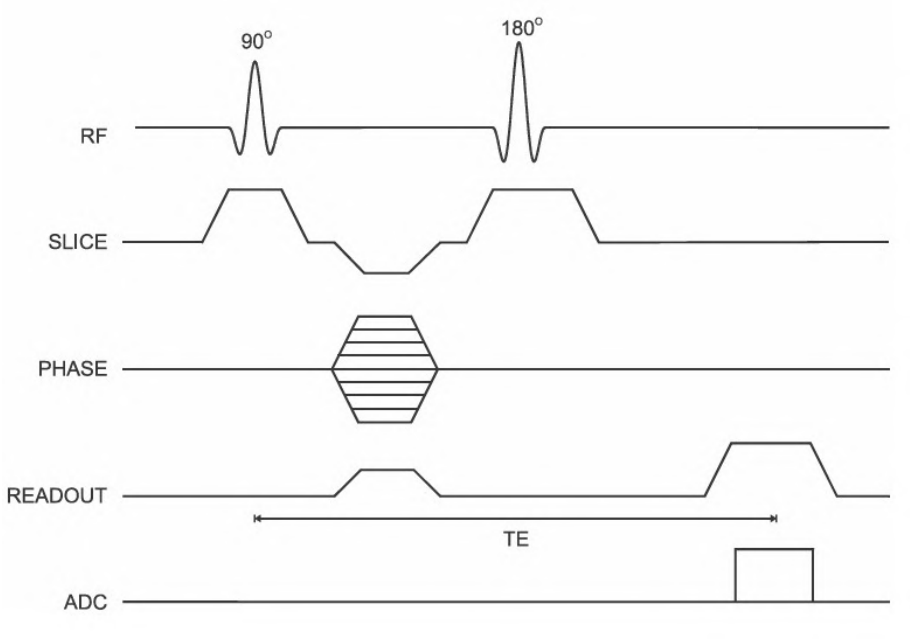

Figure 11: **Timing diagram of a Standard Single Echo Sequence** [13]
An excitation pulse is followed by a single 180° refocusing pulse resulting in a single echo. The timing of the slice-selection, phase-encoding and readout gradients is shown. The echo time is the time between centre of the excitation pulse and the middle of the echo

gradients. As well as a line indicating the moment of the echo and the echo time TE [13].

2.3 Functional Magnetic Resonance Imaging

Experiments done by Roy and Sherrington in 1890 [71] first indicated that changes in regional cerebral blood flow could reflect neuronal activity [37]. Functional magnetic resonance imaging (fMRI), as it is known today, was introduced by Ogawa et al. in 1990 [64]. It is a non-invasive imaging technique used to visualize neural activity of the human brain [79].
Increased neural activity induces a vascular hemodynamic response. This response is characterized by the blood oxygenation level dependent (BOLD) effect, used for functional brain mapping [37].

BOLD Effect

fMRI is based on the changes of local blood flow and oxygenation in the cortex due to neuronal activity. This is called the hemodynamic response [40]. Neuronal activity requires oxygen and glucose, both of which are supplied by the vascular system. Highly oxygenated blood is transported by the arterial part of the vascular system until it reaches the capillary bed. Here, oxygen is transferred to glial cells and neurons. Less oxygenated blood is then transported away from the capillary bed in the venous system. Oxygen is carried by the molecule hemoglobin, shown in Figure 12. It is called oxygenated hemoglobin (HbO_2), when it carries oxygen, and deoxygenated hemoglobin (Hb), otherwise [80]. Oxygenated and deoxygenated

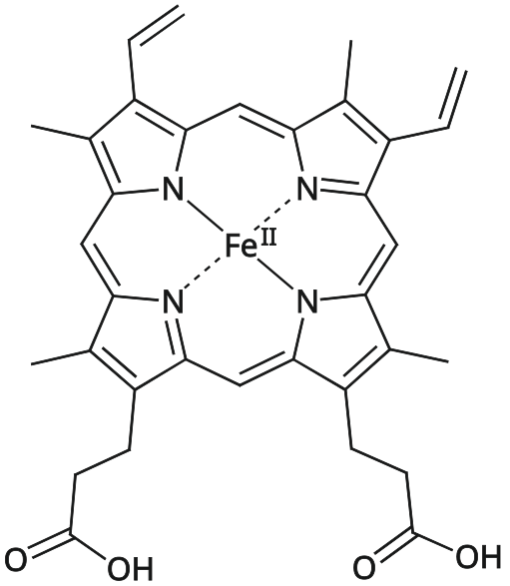

Figure 12: **Hemoglobin molecule** [84]

hemoglobin have different magnetic susceptibilities. Oxygen shields the Fe atom at the centre of the molecule, which leads to a reduction of its paramagnetic effect [16]. While the arterial part of the vascular system carries mainly oxygenated hemoglobin, the capillary bed and the venous network carry a mixture of both [80].

Figure 13 shows the hemodynamic response function (HRF). An increase in local neuronal activity increases the local oxygen demand. This reduces the relative concentration of oxygenated hemoglobin and is denoted as the initial dip. As a result, local blood flow increases. This response does not only compensate for the increased oxygen consumption, but it creates an oversupply of oxygenated hemoglobin. Post-stimulus the signal can fall below the baseline level, this is called the undershoot [80].
The probability density function (pdf) of the gamma distribution scaled by the parameter A can be used to model the HRF. This is described by: [80]

$$y(x; A, \tau, \sigma) = Ax^{\tau/\sigma - 1} \frac{e^{-x/\sigma}}{\sigma^{\tau/\sigma}\Gamma(\tau/\sigma)} \tag{25}$$

with τ and σ defining the onset and dispersion of the peak. The typically used HRF can be characterized using the difference of two gamma functions (Figure 14). While the peak and the dispersion of the positive BOLD response are modelled by the first gamma function, the second one models the undershoot response [80].

Paramagnetic, deoxygenated hemoglobin causes field distortions in the tissue surrounding the vessels [16]. This leads to quicker dephasing of the MR signal and therefore, T_2^*, and with it the signal, is reduced. Neuronal activation leads to an increase in oxygenated hemoglobin, which in turn reduces dephasing. The signal decays more slowly and more signal remains at the echo time TE. Therefore, the signal measured during an active state is slightly increased compared to the inactive state. The increase in signal intensity depends on the brain region and is in the

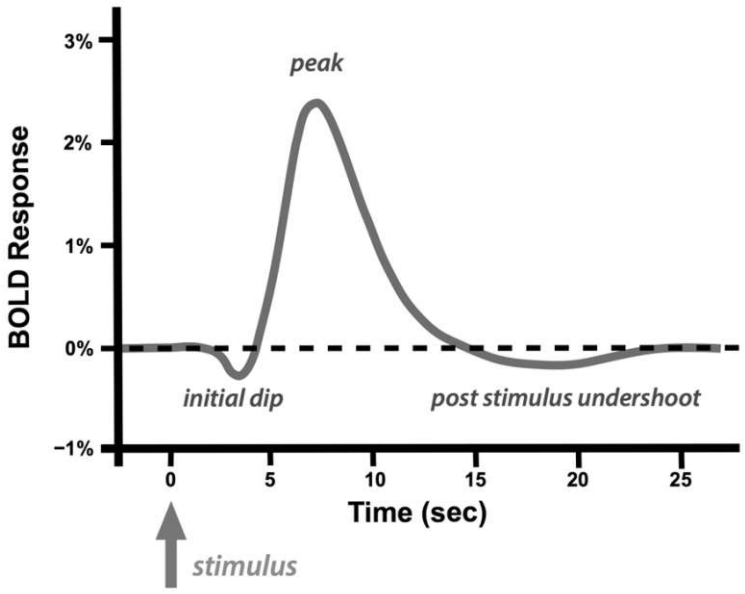

Figure 13: **Hemodynamic Response Function (HRF)** adapted from [29]
The regional BOLD response is described by the hemodynamic response function (HRF). It depicts an initial dip, followed by a peak and a variable post-stimulus undershoot [29]

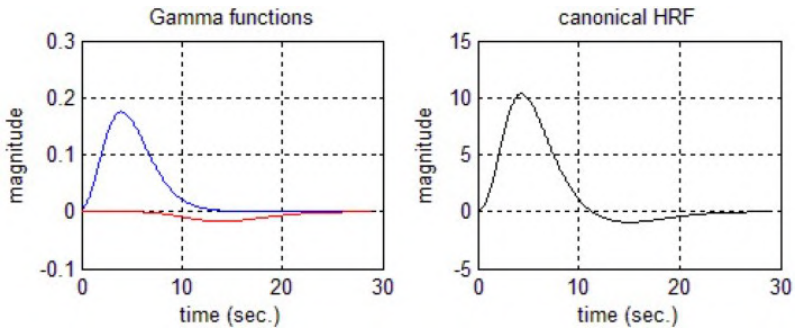

Figure 14: **Hemodynamic Response Function (HRF) modelled using two gamma functions.** Adapted from [49]
Two gamma functions (left) are subtracted from each other to model the typically used hemodynamic response function (HRF) (right) [80].

order of percent. This signal difference is the basis of the blood oxygenation level dependent contrast (BOLD), on which this fMRI technique is based [36]. For fMRI, it is necessary to cover the hemodynamic response with high temporal resolution. Thus, most applications use single-shot echo-planar imaging (EPI) for acquiring the BOLD signal. Further details to this sequence are given in the next chapter.

Echo Planar Imaging

Echo planar imaging (EPI) is a T_2^*-weighted technique, that is used to shorten acquisition times. EPI was first described by Mansfield in 1977 [59]. It was used to image a rabbit heart in 1981 [65] and to study heart defects in infants in 1983 [72]. The images in the early studies were obtained at a field strength of 0.1T [74].

In single-shot EPI the complete k-space is measured after a single excitation pulse, to shorten the acquisition times. Figure 15 shows a schematic diagram of a generic EPI pulse sequence. After excitation, two gradients are applied to get to the starting point of the first k-space line: One in the phase-encoding direction and one in the readout direction. This is followed by an oscillating gradient in readout direction to move along k_x, combined with short gradient pulses in the phase-encoding direction. The short gradient pulse shifts the current k-space location from one line to the next in the phase-encoding direction. This leads to a zig-zag k-space trajectory. At every line a gradient echo is recorded [38].

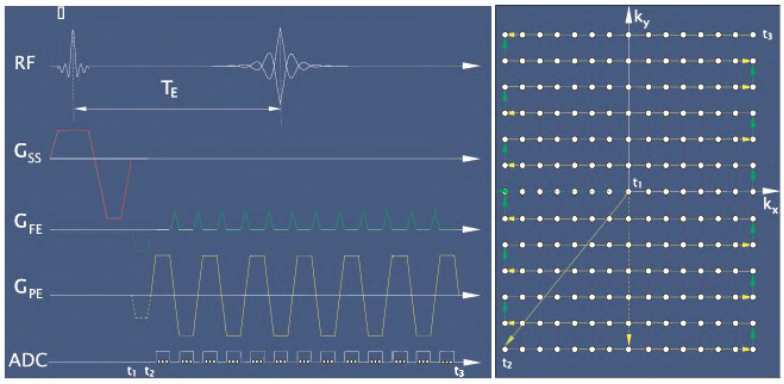

Figure 15: **Schematic Diagram of an EPI pulse sequence** [38]
When using EPI, the entire k-space is encoded in a single acquisition period. Initially two gradients are applied, one in phase-encoding and one in readout direction. An oscillating gradient in readout direction and a short gradient pulse in phase-encoding direction lead to a zig-zag trajectory through the k-space. A gradient echo is measured at every line.

2.4 The Visual System

In this thesis, fMRI is applied to the visual cortex. I will therefore use the following chapter to give a short introduction to the visual system.

Figure 16 shows a schematic image of a human eye. The anterior part of the eye contains, among other things, the cornea, the pupil, the iris and the lens. Light

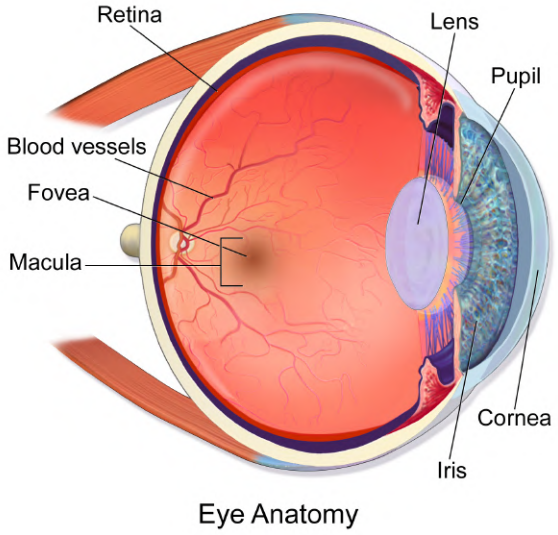

Figure 16: **Anatomy of the human eye** [78]
Schematic image of the human eye. The right side shows the cornea, pupil, iris and lens. Light passes through the cornea and pupil and the lens focuses the image on the retina. [34]

enters the eye trough the cornea and the pupil. The size of the pupil is controlled by the iris and is largely determined by the level of illumination. The lens then focuses the image on the retina at the back of the eye. In addition to the retina, the posterior part of the eye contains the fovea, the macula and the optic disc. The fovea is the area on the retina with the best spatial and colour vision. It covers an area of around 2° visual angle located around the point of fixation [34]. The fovea can be further divided into the foveal avascular zone, the foveola and the umbo (or foveal pit), the most central region of the fovea (Figure 17) [51]. The fovea is surrounded by the macula [34]. The axons of the retinal neural cells come together at the optic disc. This area doesn't contain any photoreceptor cells, and therefore forms the blind spot. The neural cells leave the eye as the optic nerve, which transmits the signal to the brain [70].

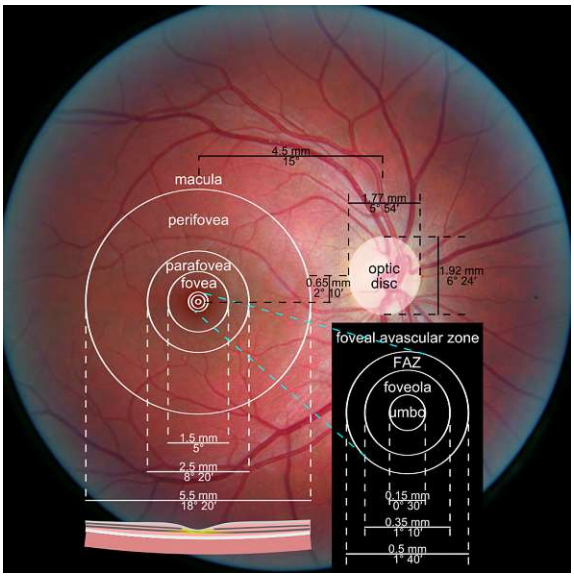

Figure 17: **Regions of the Fovea** [7]
The fovea can be further divided into the umbo, the most central region, the foveola and the foveal avascular zone (FAZ)

Retina

The retina consists of multiple layers of neural cells. The photoreceptors are connected to bipolar cells, which are again connected to ganglion cells. The axons of these ganglion cells then form the optic nerve. The photoreceptors transduce the optical image into chemical and electrical signals. These signals are then transmitted via the optic nerve. The combined signal from multiple photoreceptors provides input to ganglion cells [34].
The retina contains two classes of photoreceptors, rods and cones. Rods are active during scotopic vision, i.e. at low luminance levels. Vision at high luminance levels is called photopic vision. In this case only cones are active, while rods are effectively saturated. At intermediate luminance levels both rods and cones are active, this is referred to as mesopic vision [34].

While there is only one type of rod photoreceptor, there are three sub-types of cone receptors. They are called L- (long-wavelength-sensitive), M- (medium-wavelength-sensitive) and S- (short-wavelength-sensitive) cones and are sensitive to different parts of the visual light spectrum. The spectral sensitivity of L-, M- and S-cones peak at around 558nm, 530nm and 420nm respectively. The spectral sensitivity of rods peaks at around 495nm. They have a specific sensitivity spectrum shown in Figure 18. Figure 18 also shows the spectral sensitivities of the photo pigment melanopsin. Melanopsin is contained in the intrinsically photosensitive retina ganglion cells (ipRGCs). It can be seen that the spectral sensitivities of the individual photoreceptors overlap quite extensively [75]. While the cone types are responsible for colour vision, rods are incapable of distinguishing colours [34].

An interesting aspect of the photoreceptors is their extremely large number as well as their relative distribution in the retina. There are up to 150000 photoreceptors

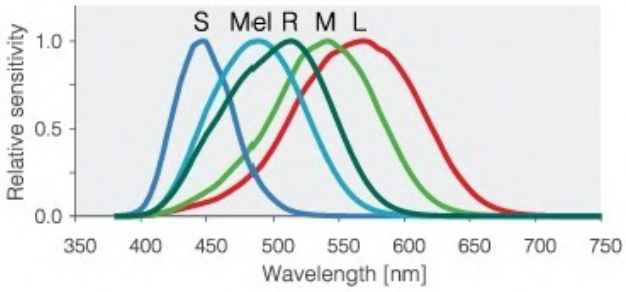

Figure 18: **Spectral sensitivities of photoreceptors of the human retina** Adapted from [75]
The spectral sensitivity of the different photoreceptors peak at different wavelengths. But there is still an extensive overlap

per square millimetre and far more rods (around 120 million per retina) than cones (around 7 million per retina). Additionally there are more L- and M-cones than S-cones. The relative population of the L:M:S cones is roughly 12:6:1. Figure 19 shows the distribution of rods and cones in the retina. In the fovea, the cones are highly concentrated and no rods are present. This allows space for the cone system to produce the highest spatial acuity. The peripheral region of the retina shows only a low number of cones. It also shows the blind spot, which is the area where the optic nerve is formed and no photoreceptors are present [34].

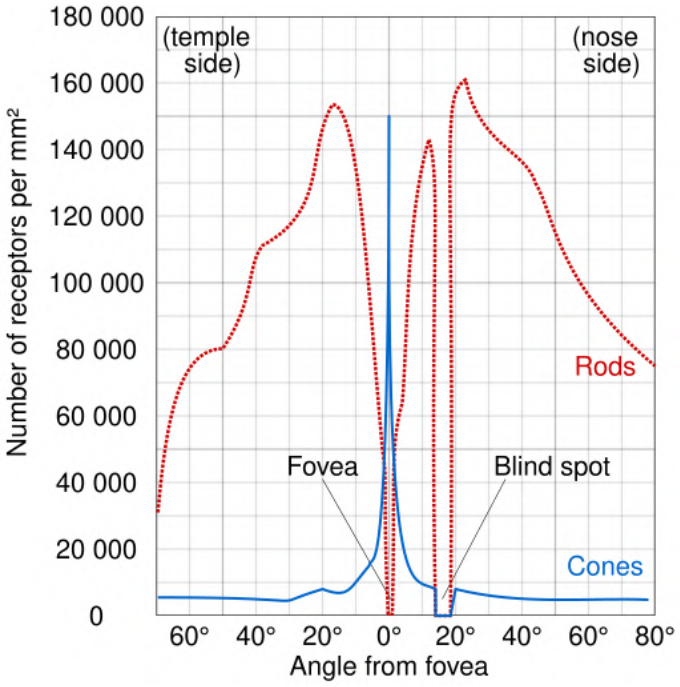

Figure 19: **Distribution of photoreceptors in the human retina** [45]
While the periphery of the retina contains more rods than cones, the fovea contains only cones. The blind spot contains no photoreceptors.

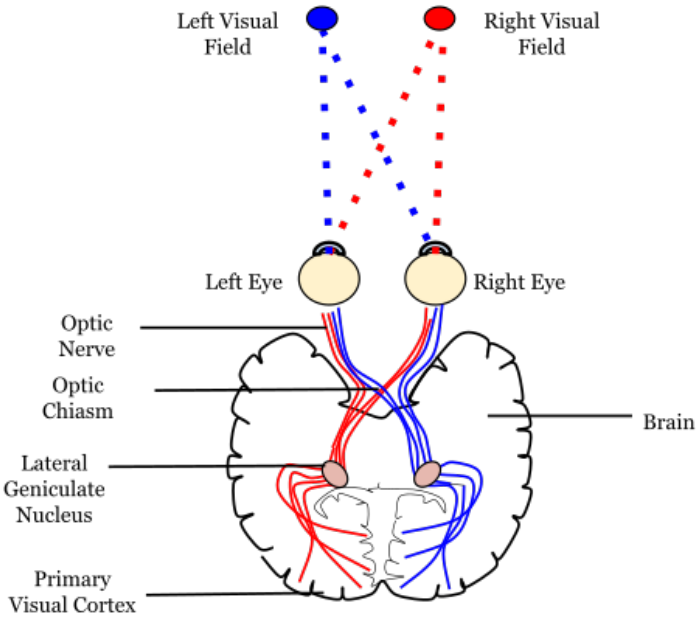

Figure 20: **Schematic diagram of the visual pathway** [58]
The optic nerves transmit the signal from the two retinae. They come together at the chiasm and are sorted into two groups. The information from the right half of the visual field is transported to the left hemisphere and vice versa for the left half. Each group connects to the lateral geniculate nucleus (LGN) of the respective hemispheres. Which then project the information to the primary visual area [34].

Visual Pathway

A schematic diagram of the visual pathway is shown in Figure 20. The optic nerves of the two retinae come together at the optic chiasm. Here the nerve fibres are rearranged into two groups, that each connect to one of the hemispheres of the brain. Information from the right half of the visual field is transported to the left hemisphere and vice versa for the left half. Therefore, both hemispheres receive information from both eyes but only from one half of the visual field [82]. The nerve fibres connect to the lateral geniculate nucleus (LGN) of the respective hemispheres. The LGN cells project the information from the optic nerve to the primary visual area (V1) in the occipital lobe of the cortex via the optic radiation [34].

Visual Cortex

The cortex of the human brain is divided into four lobes, called the frontal, parietal, temporal and occipital lobe (Figure 21). These lobes contain many distinct brain areas [82].

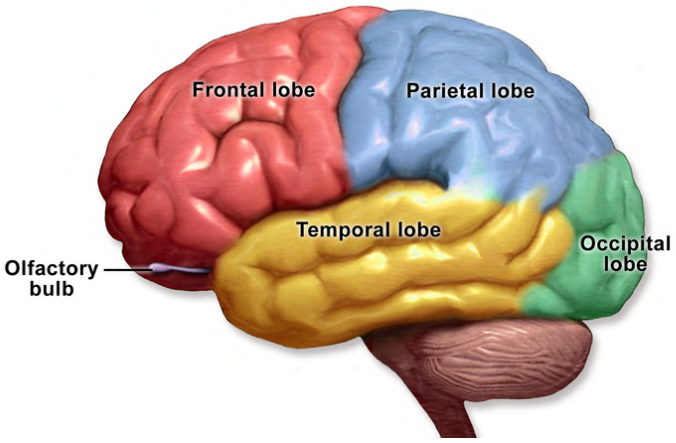

Figure 21: **Lobes of the human brain** [77]
The cortex of the brain is divided into the frontal, parietal, temporal and occipital lobe [82].

As mentioned above, the signal from the retina is transmitted to the primary visual cortex within the occipital lobe (Figure 22). While the results of this work are focussed on this area, in addition to V1 more than 20 additional visual regions (V2, V2, V4, etc.) have been discovered [82].

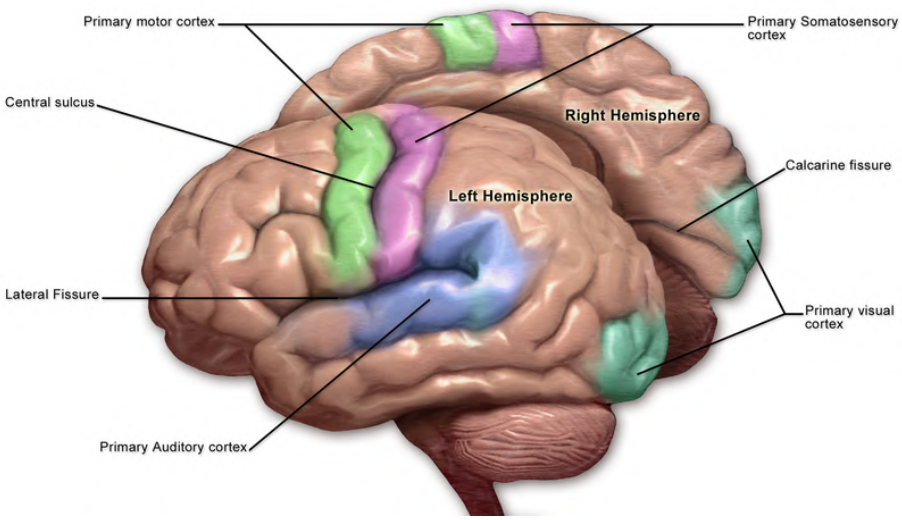

Figure 22: **Motor and sensory regions of the cerebral cortex** [76]

A significant property of the visual cortex is that the right hemisphere only receives information regarding the left half of the visual field and vice versa. Therefore, while

each LGN receives information from both eyes, they receive only information from one half of the visual field [82]. Additionally, the central region of the visual field, around the fovea, projects onto a larger region of cortical surface compared to the peripheral visual field [83]. This is called cortical magnification [25].

2.5 Retinotopic Mapping

Each cell in the visual cortex responds to an area in the visual field, and this area is represented by receptive fields [34]. Additionally, the visual cortex is organized retinotopically. Adjacent areas in the visual field project to adjacent areas on the visual cortex. This retinotopic organization means adjacent neurons have receptive fields with nearby locations in the image [83].

Retinotopic maps are defined with respect to a fixation point. Everything to the right of the fixation point is in the right visual field, everything below is in the lower field and so on. This entails, that the visual field shifts with the eye position. A way to measure retinotopic maps is by measuring the location of a stimulus that results in the largest cortical response. This can be done by using different types of stimuli. Typical examples are ring, wedge or bar stimuli, which reveal a high-contrast pattern as they move trough the visual field (Figure 23) [83].

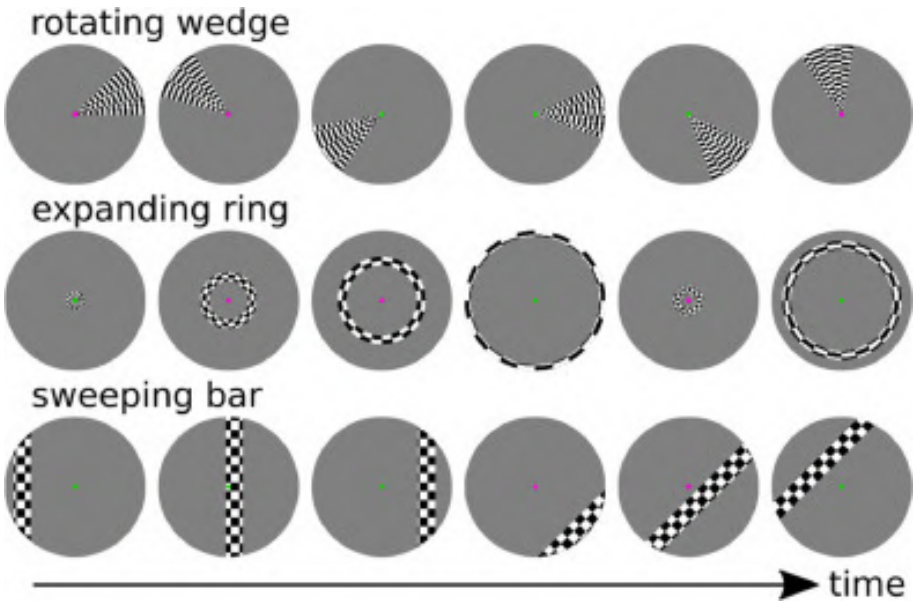

Figure 23: **Different types of stimuli** [57]
Here one can see examples of typically used stimuli, From top to bottom: wedge, ring and bar stimulus.

These stimuli are used to measure the coordinates (eccentricity and angle) of the visual field position. Figure 24 shows an example of a retinotopic map of the right hemisphere. It shows that the most posterior region of the visual cortex corresponds to the central region of the visual field. And everything in the upper/lower visual field corresponds to the lower/upper bank of the primary visual cortex [83].

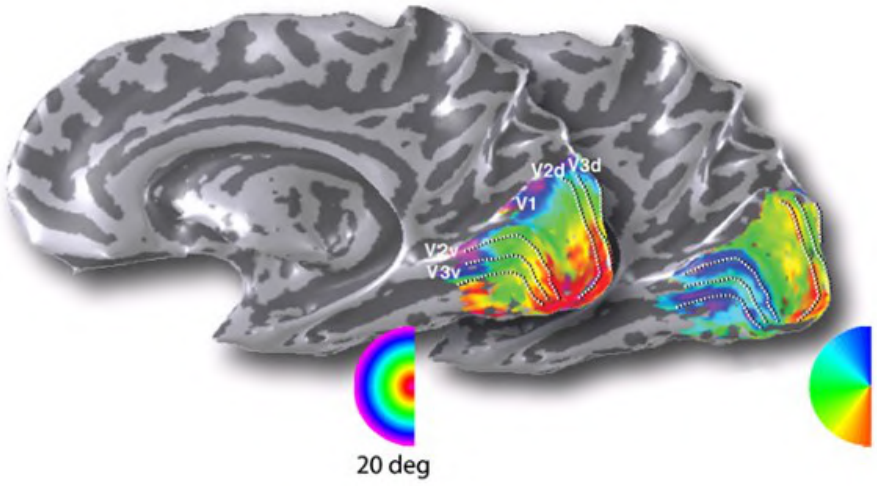

Figure 24: **Retinotopic Map** [83]

Population Receptive Field

A population receptive field (pRF) is the region of visual space that elicits a response of a neuronal population within a voxel. pRF mapping can be performed with functional MRI and as such is a non-invasive method to study retinotopic organisation. Functional images of the visual cortex are acquired while participants are shown a stimulus. The area in the visual field that leads to a response in the individual voxel is then modelled as a two dimensional Gaussian function. The Gaussian function is defined by three parameters x_0, y_0 and σ. x_0 and y_o are the centre position in the visual field and σ is the pRF size (or Gaussian spread). The predicted time series depends on the pRF model, the stimulus and the hemodynamic response function (HRF). The optimal pRF parameters are found by comparing the predicted time series with the obtained data to find the best fit [28].

In addition to retinotopic maps, the pRF method is able to estimate other population properties such as pRF size. This estimation can be affected by a number of unwanted factors: eye movements, head movements, brain pulsatility and optical defocus. These factors lead to a larger size estimate. But the most important influence is the HRF, with the the choice of HRF influencing the estimated pRF size [28].

2.6 Silent Substitution

The method of silent substitution can be traced back to the early 1900s, where it was first used by Makoto Ishihara [47]. It was further established by the work of Donner and Rushton in 1959 [27].

As mentioned in chapter 2.4, photoreception is based on the two types of photoreceptors (rods and cones) in the retina, with one type of rods and three types of cones. All photoreceptors have different, but overlapping, spectral sensitivities (Figure 18). This overlap makes is challenging to target a single type of photoreceptor, since

most light sources activate all photoreceptors. Even monochromatic light at the peak spectral output of rods (495nm) will activate L-cones and M-cones as well. A way to circumvent this problem is by exploiting a property of the photoreceptors called the principle of univariance. It is based on finding two wavelengths of light where one type of photoreceptor perceives a difference, while the excitation of the other type of photoreceptor remains constant. The photoreceptor with constant excitation is thereby silenced. When using silent substitution, pairs of light, the background and the modulation spectrum, are used to target one photoreceptor, while not stimulating the other ones. To achieve this, the number of primary lights must match the number of photoreceptors [75].

3 Stimulus Design

In this thesis, we intended to selectively activate rod or cone photoreceptors. To achieve this, we chose the method of silent substitution. This method is based on the inability of photoreceptors to distinguish between changes in wavelength and changes in intensity. It uses a chromatic pair, a background and a modulation colour, to activate one type of photoreceptor, while silencing the others [75].

3.1 Calibration

To determine the modulation and background colour, i.e. the RGB (Red Green Blue) values suitable for our setup, the python package PySilSub (`https://github.com/PySilentSubstitution/pysilsub`) [61] was used. For this package to work, it is necessary to acquire an accurate set of calibration measurements for the respective projector setup. To acquire these calibration measurements we rebuilt the setup used in the scanner, using the same mirrors and distances, outside the scanner room. The measurements were performed at night, in order to avoid light sources other than the projected light to influence the measurements. The spectrometer CSS110 (Thorlabs, USA) was used in combination with the Thorlabs ThorSpectra software to measure the light spectrum.

Before the actual calibration data was measured, a series of preliminary tests was performed. A simplified setup was built using a projector and the same screen used in the fMRI setup. Full-field images were projected onto the screen for each of the three individual RGB values. The RGB colour model is an additive system, where the wavelengths of its primary colours (red, green and blue) are combined to create a vast range of colours. If all three colours are added together at full intensity white is generated. This system is used in digital devices, such as monitors or projectors, to generate a multitude of colours on screens [85].
In this case, the spectra of the individual RGB values were measured at maximum intensity (Figure 25). The measured shape matches the expected projector output.

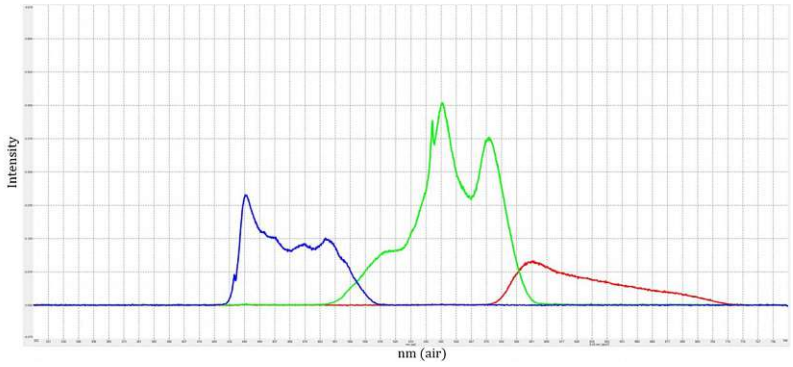

Figure 25: **Results of initial spectrometer test**
The spectra for the individual RGB values are shown at maximum intensity. The colour of the curve corresponds to the respective RGB value. The shape corresponds to what we would expect from the projector output.

For the measurements of the actual calibration matrix, the MR setup was recreated. The RGB images were projected onto the screen via the same mirrors used during the experiment. A custom python script, based on a Thorlabs example (`https://github.com/Thorlabs/Light_Analysis_Examples`), was used to automate the projection of the images as well as the recording of the respective spectra. Additionally, the script saved the recorded data in the format required for the calibration matrix. The measurements were performed multiple times, with and without an aperture. The aperture is needed to reduce the brightness of the image produced by the projector, to avoid blinding the participants.
While the overall shape of the spectra stayed consisted, the strength of the signal was greatly reduced when comparing the results with and without aperture. This reduction of the signal reduces in turn the signal-to-noise ratio (SNR) (Figure 26).

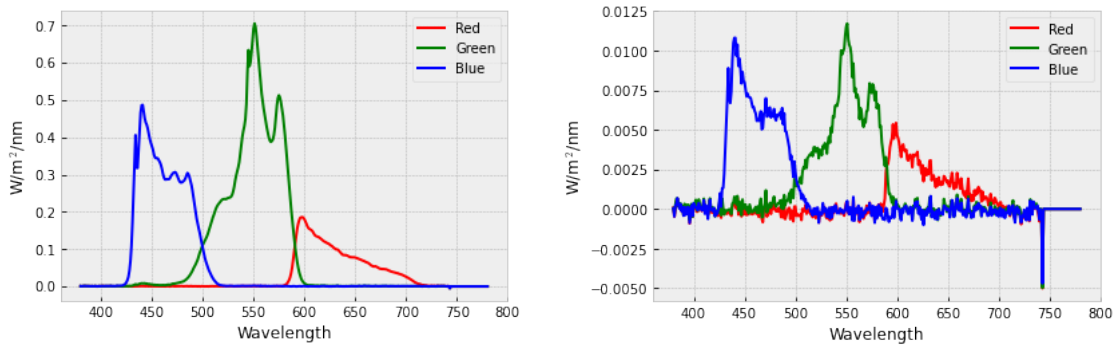

(a) Without aperture

(b) With aperture

Figure 26: **RGB spectrum at maximal intensity**
The shape of the individual spectra stayed consistent when comparing the results with and without aperture. When using the aperture, the signal is reduced, reducing the SNR.

3.2 Generating Chromatic Pairs

The data from five spectral measurements was averaged and used to generate the calibration matrix. To calculate the background and the modulation spectra, the feature 'silent substitution problems' was used. During this, the activation level for each photoreceptor subtype (E_α) was calculated. To activate only rods, the parameters were set to target rods and silence L- and M-cones. The target contrast was set to 0.5. To activate only cones, L- and M-cones were targeted and rods were silenced, with maximum contrast. Melanopsin and S-cones were set to be ignored in both conditions. The results were obtained using global optimization. For the rod-selective stimulus, the activation of L- and M-cones (E_{lc} and E_{mc}) stays constant for the background and modulation spectrum (Figure 27, left). And for the cone-selective stimulus the difference in activation for rods (E_{rh}) is very small (Figure 27, right).

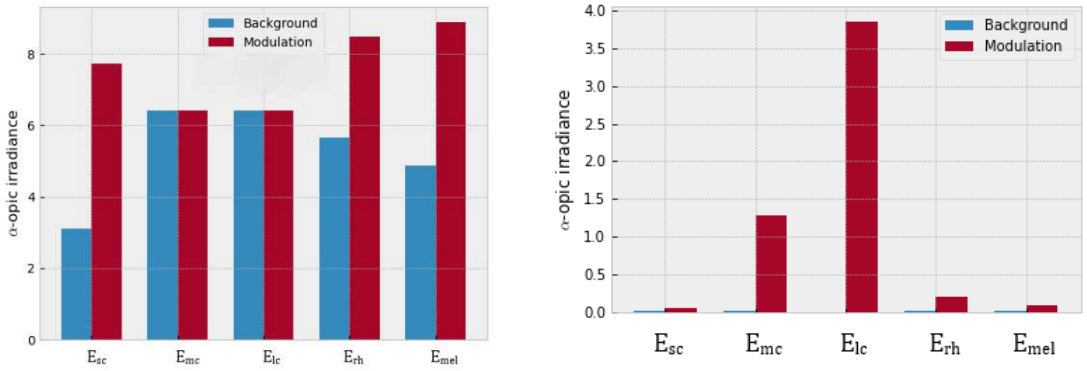

(a) Rod-selective result

(b) Cone-selective result

Figure 27: **Optimization Results**
The results for rod-selective (left) and cone-selective (right) optimization. The activation levels for L- and M-cones (E_{lc} and E_{mc}) stay constant for the rod-selective stimulus. For the cone-selective stimulus the difference in activation for rods (E_{rh}) is very small.

The resulting values were used to generate two stimuli, each consisting of a respective background and modulation colour. Figures 28a and 28b show the chromatic pairs used to selectively activate rods or cones.

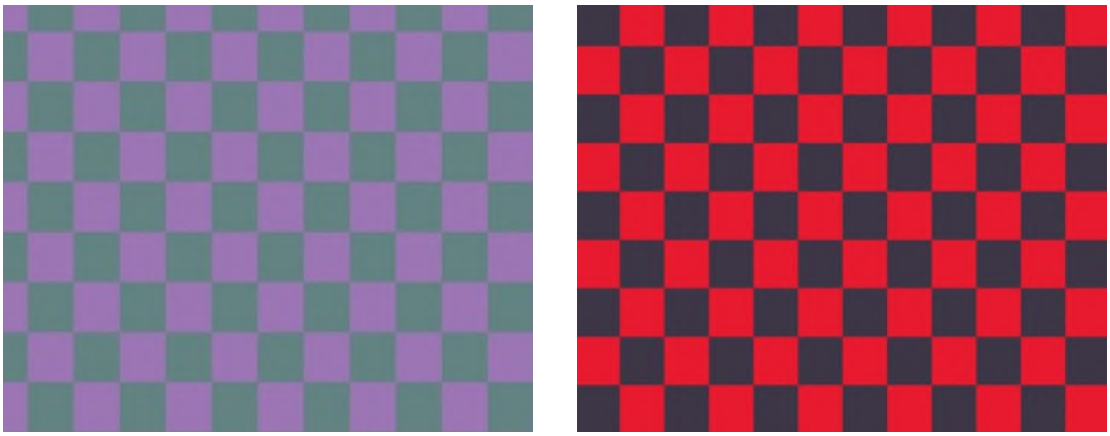

(a) Rod activation

(b) Cone activation

Figure 28: **Colour combination to activate rods and cones individually**

3.3 Measurement Conditions

In addition to the stimuli, the measurement conditions themselves were also taken into account. We reduced the illumination levels inside the scanner room by covering all light sources. This was done to ensure scotopic vision, a state at low luminance levels, were only rods are active, and cones are insensitive. In addition to illumination levels, we also considered dark adaptation. This is the change in visual sensitivity which occurs when the light levels are decreased. This takes about 30 minutes and results in the visual system being more sensitive at lower illumination

levels [34]. The participants spent 30 minutes inside the dark scanner room to establish dark adaptation, before the functional measurements were performed. During the functional measurements, the details of which are explained in Chapter 4.2, we used neutral density (ND) filters to reduce the brightness of the projected images and therefore, to maintain scotopic vision. ND filters reduce the brightness of the image without altering the projector spectrum. The ND filters were used in addition to the aperture, that was already placed on the projector. Two luminance levels were created using a ND512 and a ND256 filter. The two strengths were achieved by combining a ND64 filter with a ND8 and a ND4 filter respectively. The filters were placed on top of the aperture.

For the measurements were cones were activated, the goal was to achieve photopic vision, a state were only cones are active and rods are saturated. Photopic vision occurs during bright light conditions [34]. Therefore no filters were used to dim the brightness of the projected image. But we still used the aperture, otherwise the light would be too bright.

4 Methods

4.1 Subjects

Seven subjects were measured, four female and three male at a mean age of 26.57 $\pm$ 2.76 years. Subjects were provided with information regarding their tasks only shortly before the session and had no previous knowledge. The subjects had no history of eye disease. They provided informed written consent and were compensated financially for their participation.

4.2 MR Measurements

The measurements were obtained on a 3T SIEMENS Prisma-Fit scanner using a 64-channel head-coil. Each subject participated in a single session. Before the functional measurements, the participants spent 30 minutes in the dark scanner room. During this dark adaptation period, a structural T1-weighted MP2RAGE image was acquired, with a spatial resolution of 1mm isotropic and the following set of parameters: TE = 2.98ms, TR = 4000ms, field of view = 216 x 256mm, number of slices = 160, inversion time 700ms and 2500ms. For the acquisition of the structural image, the full 64-channel head-coil were used.

Three illumination levels were generated by using either a ND512 filter, a ND256 filter or no filter. At each brightness level a set of three functional runs was recorded. During the first measurements, Study 1, five participants were measured. The first two functional sets were measured using the rod-selective stimulus. First using the ND512 filter and then using the ND256 filter. The third set was acquired using the cone-selective stimulus without a filter. A second set of measurements, Study 2, was performed with three participants, one of which also participated in the first set. Three sets of functional runs were recorded were the order of the stimuli was switched. The first two functional sets, using the ND512 and the ND256 filter, were

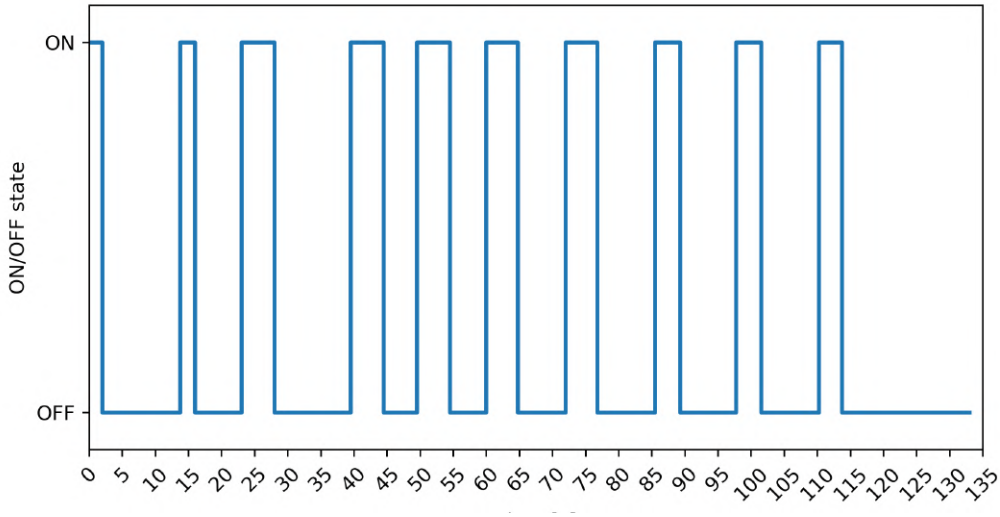

Figure 29: **Time course of the full-field stimulus**

recorded using the cone-selective stimulus. And the third set, without a filter, was recorded using the rod-selective stimulus.
For the functional runs, only the posterior part of the head coil was used. A custom screen was mounted inside the bore on the end of the patient table. The light from the projector was projected onto this screen via a mirror. The second mirror, placed over the participants head, allowed them to see the screen. The participants were shown a fixation cross, centred in the centre of the visual field. They were instructed to fixate the centre of the cross and to press a button as a response to it changing colour. The eyetracker EyeLink 1000 Plus (SR Research, Ottawa, ON) was used to manually track the participants state of alertness. This, combined with the participants response to the colour change was used to assess compliance.

Functional data was acquired using the CMRR EPI sequence [63] with a spatial resolution of 1.5mm isotropic and the following parameters: TE = 38ms, TR = 1000ms, matrix size = 80 x 80, field of view = 120 x 120mm, flip angle = 55°, simultaneous multislice = 3, partial fourier = $\frac{6}{7}$, effective echo spacing = 1.01ms, phase encoding direction = left-to-right, slice spacing = 10%. The measured volume consisted of 30 slices of the occipital pole region which were aligned parallel to the calcarine sulcus.

During the first run of each functional set, the participants were shown a full-field stimulus. The stimulus revealed a checkerboard pattern, covering the whole visual field. While, the pattern flickered continuously on and off, the duration of the individual 'ON' states varied (Figure 29). Table 1 shows the time points for the individual onsets as well as the duration of the respective 'ON' states. The complete run lasted for 133 volumes, resulting in a duration of 2 minutes and 13 seconds.

The remaining set consists of two runs using a bar stimulus. The bar revealed a checkerboard pattern and moved across the field of view in eight different directions.

Onset	Duration [s]
0.00	2.00
13.75	2.25
23.00	5.00
39.50	5.00
49.50	5.00
60.00	4.75
72.00	4.75
85.50	3.75
97.75	3.75
110.25	3.50

Table 1: **Onset and duration of 'ON' states of the full-field stimulus**

It had a width of 1.6° and the stimulus reached a total diameter of 18° visual angle. After each pass through the visual field, the bar rotated by 45° and after each diagonal crossing there were 12s of baseline. The bar jumped once per TR for $\frac{1}{2}$ of the bar width. Each run lasted for 240 volumes, resulting in a duration of 4 minutes.

4.3 Analysis

The first step in the analysis was the pre-processing. Results included in this manuscript come from preprocessing performed using *fMRIPrep* 23.0.1 ([33]; [32]; RRID:SCR_016216), which is based on *Nipype* 1.8.5 ([42]; [43]; RRID:SCR_002502) (`https://fmriprep.org/en/stable/`).

Preprocessing of B0 inhomogeneity mappings A total of 1 fieldmaps were found available within the input BIDS structure for this particular subject. A *B0*-nonuniformity map (or *fieldmap*) was estimated based on two (or more) echo-planar imaging (EPI) references with `topup` ([2]; FSL 6.0.5.1:57b01774).

Anatomical data preprocessing A total of 1 T1-weighted (T1w) images were found within the input BIDS dataset.The T1-weighted (T1w) image was corrected for intensity non-uniformity (INU) with `N4BiasFieldCorrection` [81], distributed with ANTs 2.3.3 [3, RRID:SCR_004757], and used as T1w-reference throughout the workflow. The T1w-reference was then skull-stripped with a *Nipype* implementation of the `antsBrainExtraction.sh` workflow (from ANTs), using OASIS30ANTs as target template. Brain tissue segmentation of cerebrospinal fluid (CSF), white-matter (WM) and gray-matter (GM) was performed on the brain-extracted T1w using `fast` [FSL 6.0.5.1:57b01774, RRID:SCR_002823, 86]. Brain surfaces were reconstructed using `recon-all` [FreeSurfer 7.3.2, RRID:SCR_001847, 19], and the brain mask estimated previously was refined with a custom variation of the method to reconcile ANTs-derived and FreeSurfer-derived segmentations of the cortical gray-matter of Mindboggle [RRID:SCR_002438, 50]. Volume-based spatial normalization to one standard space (MNI152NLin2009cAsym) was performed through nonlinear registration with `antsRegistration` (ANTs 2.3.3), using brain-extracted

versions of both T1w reference and the T1w template. The following template was were selected for spatial normalization and accessed with *TemplateFlow* [23.0.0, 17]: *ICBM 152 Nonlinear Asymmetrical template version 2009c* [[39], RRID:SCR_008796; TemplateFlow ID: MNI152NLin2009cAsym].

Functional data preprocessing For each of the 9 BOLD runs found per subject (across all tasks and sessions), the following preprocessing was performed. First, a reference volume and its skull-stripped version were generated by aligning and averaging 1 single-band references (SBRefs). Head-motion parameters with respect to the BOLD reference (transformation matrices, and six corresponding rotation and translation parameters) are estimated before any spatiotemporal filtering using `mcflirt` [FSL 6.0.5.1:57b01774, 48]. The estimated *fieldmap* was then aligned with rigid-registration to the target EPI (echo-planar imaging) reference run. The field coefficients were mapped on to the reference EPI using the transform. BOLD runs were slice-time corrected to 0.441s (0.5 of slice acquisition range 0s-0.882s) using `3dTshift` from AFNI [18, RRID:SCR_005927]. The BOLD reference was then co-registered to the T1w reference using `bbregister` (FreeSurfer) which implements boundary-based registration [44]. Co-registration was configured with six degrees of freedom. First, a reference volume and its skull-stripped version were generated using a custom methodology of *fMRIPrep*. Several confounding time-series were calculated based on the *preprocessed BOLD*: framewise displacement (FD), DVARS and three region-wise global signals. FD was computed using two formulations following Power (absolute sum of relative motions, [67]) and Jenkinson (relative root mean square displacement between affines, [48]). FD and DVARS are calculated for each functional run, both using their implementations in *Nipype* [following the definitions by 67]. The three global signals are extracted within the CSF, the WM, and the whole-brain masks. Additionally, a set of physiological regressors were extracted to allow for component-based noise correction [*CompCor*, 5]. Principal components are estimated after high-pass filtering the *preprocessed BOLD* time-series (using a discrete cosine filter with 128s cut-off) for the two *CompCor* variants: temporal (tCompCor) and anatomical (aCompCor). tCompCor components are then calculated from the top 2% variable voxels within the brain mask. For aCompCor, three probabilistic masks (CSF, WM and combined CSF+WM) are generated in anatomical space. The implementation differs from that of Behzadi et al. in that instead of eroding the masks by 2 pixels on BOLD space, a mask of pixels that likely contain a volume fraction of GM is subtracted from the aCompCor masks. This mask is obtained by dilating a GM mask extracted from the FreeSurfer's *aseg* segmentation, and it ensures components are not extracted from voxels containing a minimal fraction of GM. Finally, these masks are resampled into BOLD space and binarized by thresholding at 0.99 (as in the original implementation). Components are also calculated separately within the WM and CSF masks. For each CompCor decomposition, the k components with the largest singular values are retained, such that the retained components' time series are sufficient to explain 50 percent of variance across the nuisance mask (CSF, WM, combined, or temporal). The remaining components are dropped from consideration. The head-motion estimates calculated in the correction step

were also placed within the corresponding confounds file. The confound time series derived from head motion estimates and global signals were expanded with the inclusion of temporal derivatives and quadratic terms for each [73]. Frames that exceeded a threshold of 0.5 mm FD or 1.5 standardized DVARS were annotated as motion outliers. Additional nuisance timeseries are calculated by means of principal components analysis of the signal found within a thin band (*crown*) of voxels around the edge of the brain, as proposed by [66]. The BOLD time-series were resampled into standard space, generating a *preprocessed BOLD run in MNI152NLin2009cAsym space*. First, a reference volume and its skull-stripped version were generated using a custom methodology of *fMRIPrep*. The BOLD time-series were resampled onto the following surfaces (FreeSurfer reconstruction nomenclature): *fsnative*, *fsaverage*. All resamplings can be performed with *a single interpolation step* by composing all the pertinent transformations (i.e. head-motion transform matrices, susceptibility distortion correction when available, and co-registrations to anatomical and output spaces). Gridded (volumetric) resamplings were performed using `antsApplyTransforms` (ANTs), configured with Lanczos interpolation to minimize the smoothing effects of other kernels [52]. Non-gridded (surface) resamplings were performed using `mri_vol2surf` (FreeSurfer).

Many internal operations of *fMRIPrep* use *Nilearn* 0.9.1 [1, RRID:SCR_001362], mostly within the functional processing workflow. For more details of the pipeline, see the section corresponding to workflows in *fMRIPrep*'s documentation (`https://fmriprep.readthedocs.io/en/latest/workflows.html`).

In the next step the data was prepared for the analysis using the containerized tool prfprepare v1.4.3 (`https://github.com/fmriat/prfprepare`) [57]. This tool uses stimulus images and vistadisp log files to build the stimulus. The areas were then masked to the surface and the bold files, containing the preprocessed data were then converted to 2D NIFIT2 files. The correct stimulus appertures were then linked to the respective bold files [26].

Following this, the data was analysed. The data from the bar stimulus was analysed using the vistalab tool prfanalyze-vista v2.1.3_3.1.2 (`https://github.com/vistalab/PRFmodel`) [54]. In the course of this analysis, a pRF model is created based on the stimulus time course, which is zero if no stimulus is present and one if there is a stimulus. This model is then folded with the hemodynamic response function (HRF). The voxels are modelled as a two-dimensional Gaussian function, with two parameters, x and y, giving the central position and one parameter, σ, giving its width. The parameters with the best fit are found by minimizing the residual sum of squares between the measured and the predicted time course.
The data from the full-field stimulus was analysed using a custom python script using nilearn v0.10.4 general linear model (`https://github.com/nilearn/nilearn`). A first level generalized linear model (GLM) is the traditional method to analyse fMRI data [41]. Initially, the model time course is created using the timing of the stimulation and baseline periods. Next, this time course is correlated with each measured voxels time course and a contrast between activation and baseline is calculated. The contrast is a weighted combination of the estimated effects. To detect

voxels with significant effect, a t-statistic is performed [46]. The results are then saved to a BIDS format for further visualization.

The pRF results were additionally handled using PRFclass (`https://github.com/dlinhardt/PRFclass`). This is used to mask the data to the primary visual cortex V1. The data from the bar as well as the full-field stimulus were then visualized using custom python scripts and prfresult v0.1.2 (`https://github.com/fMRIat/prfresult`). Cortex maps were generated, displaying the regions of activation in the primary visual cortex.

5 Results

5.1 Study 1

Low Luminance Levels

Cortical activation maps were generated, illustrating regions of the primary visual cortex (V1) that were active during the functional stimulation. Figure 30 presents the results of the functional runs using the rod-selective stimulus at low luminance levels. The upper row shows the averaged results of the two pRF runs and the lower row shows the results of the one run using the full-field stimulus.
The first two columns show the activation in the left and right hemisphere, using the ND512 filter. The third and fourth column show the activation, using the ND256 filter. Figures 30a to 30e display the results for subjects one to five, which were measured in the first study.

These results show that mainly voxels in the anterior parts of the primary visual cortex were activated (blue to violet regions in Figure 30), which corresponds to the peripheral region in the visual field. Activation in the posterior parts of the primary visual cortex (orange to red regions in Figure 30), which corresponds to the central region of the visual field, is very low. Activation increases only slightly when using the ND256 filter, i.e. with slightly higher stimulus luminance levels. Activation remains localized to the anterior regions of V1, for both the bar and the full-field stimulus. The distribution of the activation aligns with the distribution of rods on the retina (Figure 19), suggesting predominantly rod activation.

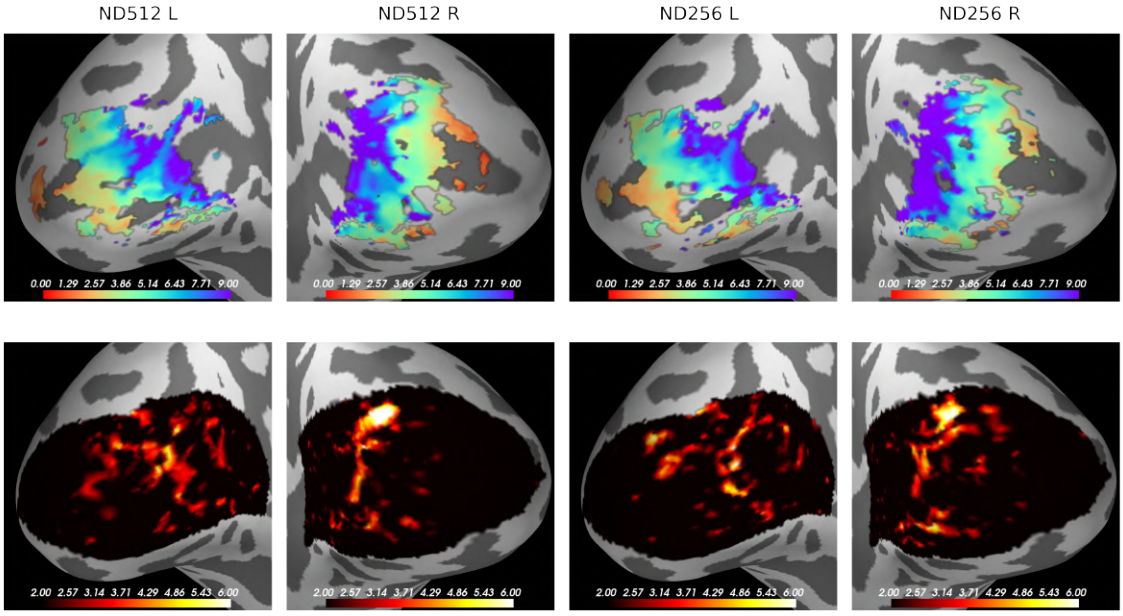

(a) Subject 1

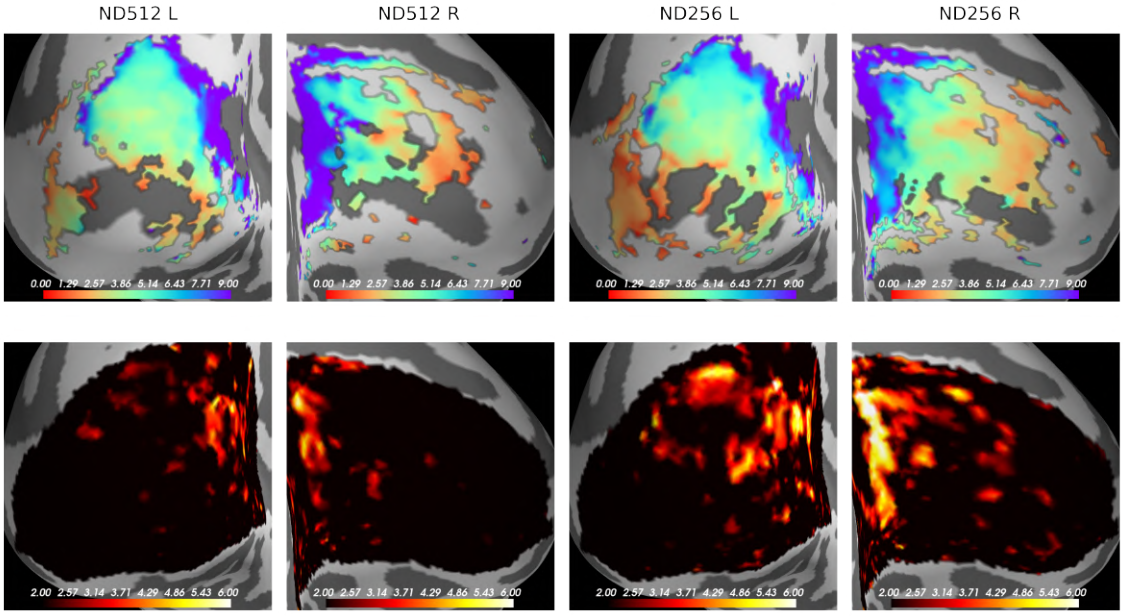

(b) Subject 2

Figure 30: **Results for rod-selective stimulus at low luminance levels**
Maps of the primary visual cortex show the regions of activation. The first two columns show results from using the rod-selective stimulus in combination with the ND512 filter. The third and fourth column show the resulting activation in V1, when using the ND256 filter. Results are displayed for all five subjects that where measured in Study 1 (Figure 30a to 30e).
While the amount of activation in the posterior region of V1 is low for both conditions, a slight increase in activation can be seen when using the ND256 filter. The activated areas correspond with the distribution of rods on the retina, indicating that primarily rods were activated.

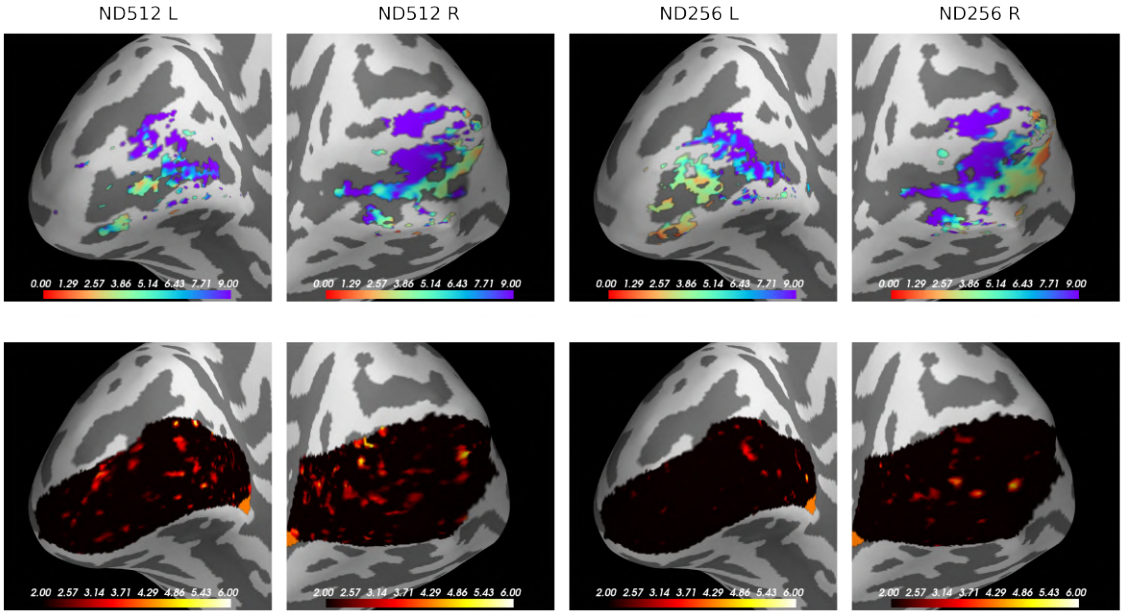

(c) Subject 3

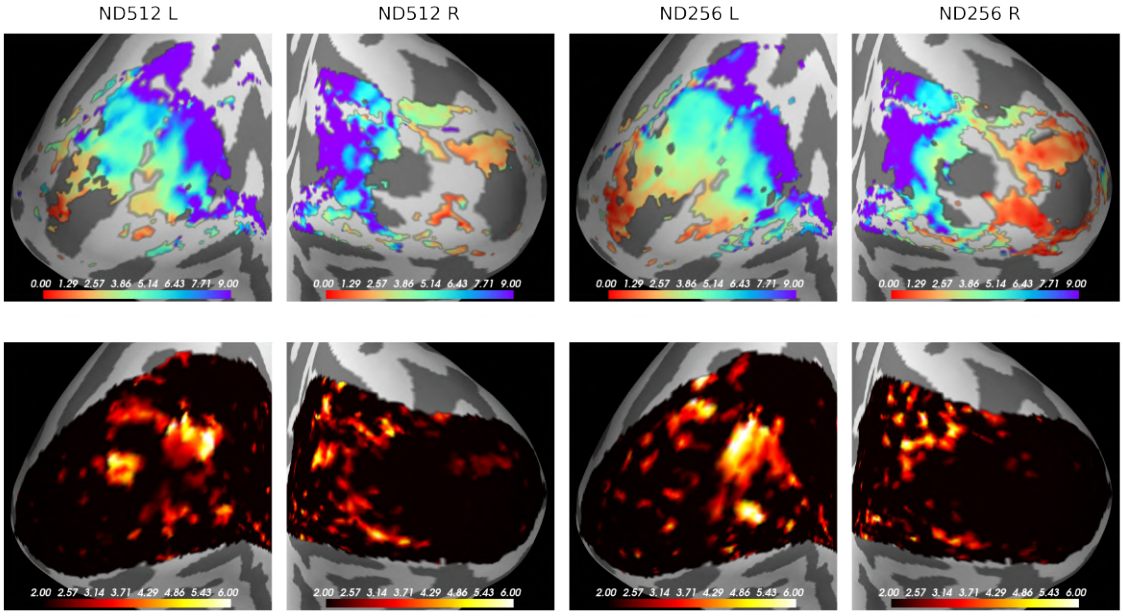

(d) Subject 4

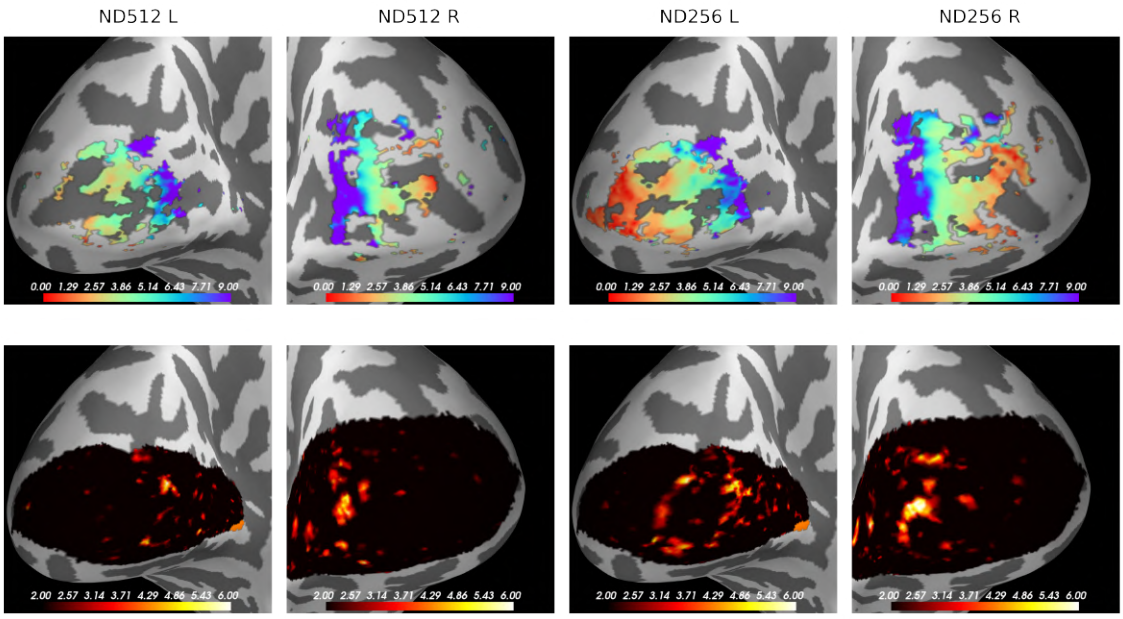

(e) Subject 5

High Luminance Levels

Figure 31 shows the activated regions in V1 for the left and the right hemisphere, corresponding to the use of the cone-selective stimulus at full brightness. As with Figure 30, the upper row shows the averaged results of the two runs using the bar stimulus and the lower row shows the results of using the full-field stimulus. The results are displayed for each subject individually (Figure 31a to Figure 31e).

Figure 31 shows a lot more activation across the whole primary visual cortex. But the increase in activation is especially noticeable for the posterior region of V1, which corresponds to the central visual field. The increase in activation is clearly visible for the pRF results as well as the results of the full-field stimulus. The activation across V1 aligns with the distribution of the cones on the retina. Especially the activation of the posterior part of V1, which corresponds to the central visual field. The strong activation corresponding to the central visual field aligns with the location of cones on the fovea. A region on the retina, where only cones are present. This suggests the activation of cones during these measurements.

While the overall results are consistent, subject-specific differences can be observed. Compared to the other participants, Figures 30c and 31c show less activation for subject three, for all tasks.

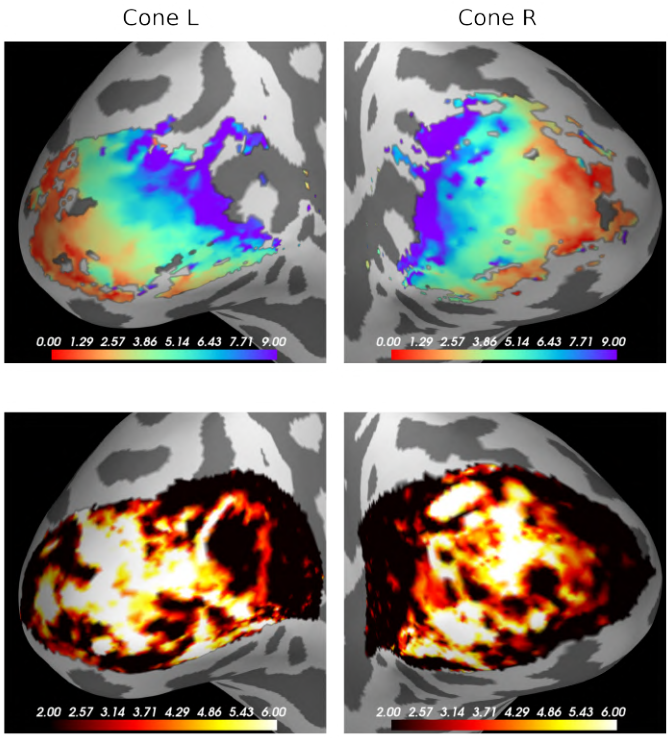

(a) Subject 1

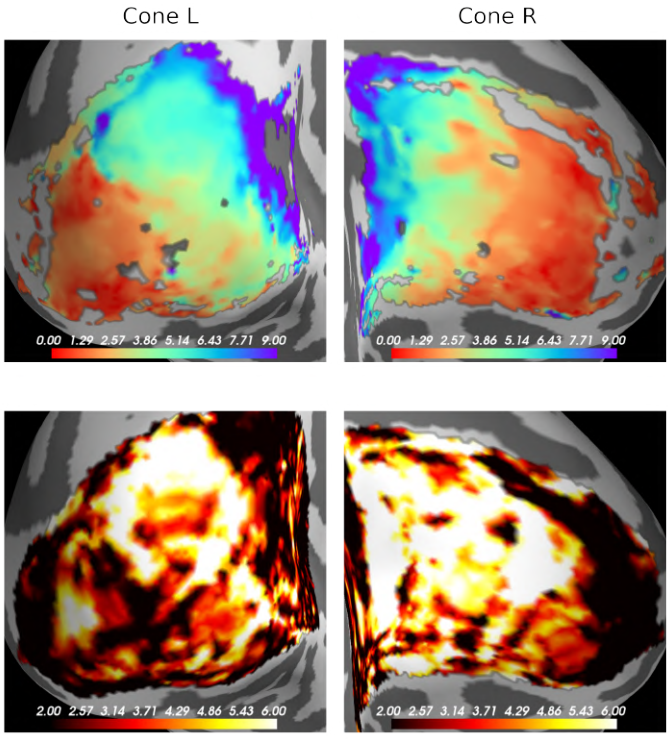

(b) Subject 2

Figure 31: **Results for cone-selective stimulus at high luminance levels** Figures 31a to 31e show activation maps of V1 for the left and right hemisphere recorded during the use of the cone-selective stimulus at full brightness levels. Activation increases considerably across the entire primary visual cortex for both functional measurements compared to low-luminance stimulation. Especially the activation in the posterior region, which corresponds with the central visual field, indicates the activation of cones.

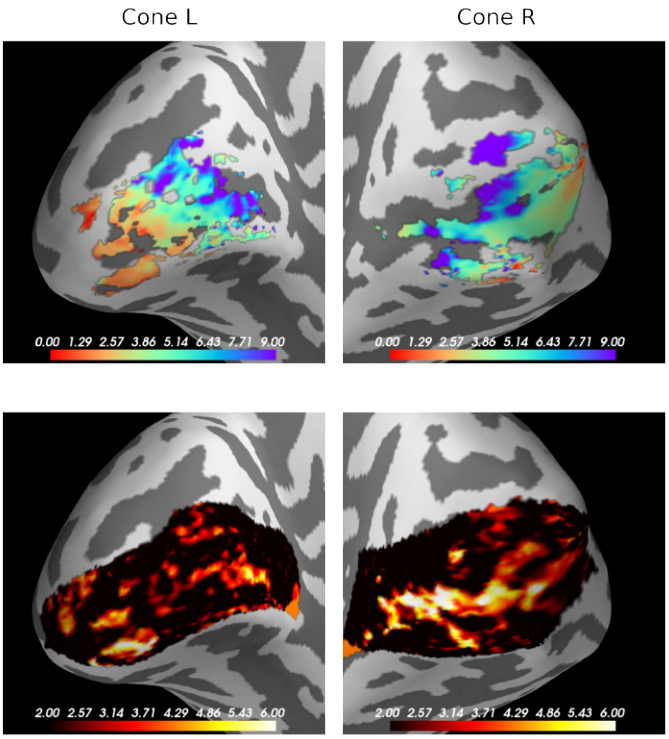

(c) Subject 3

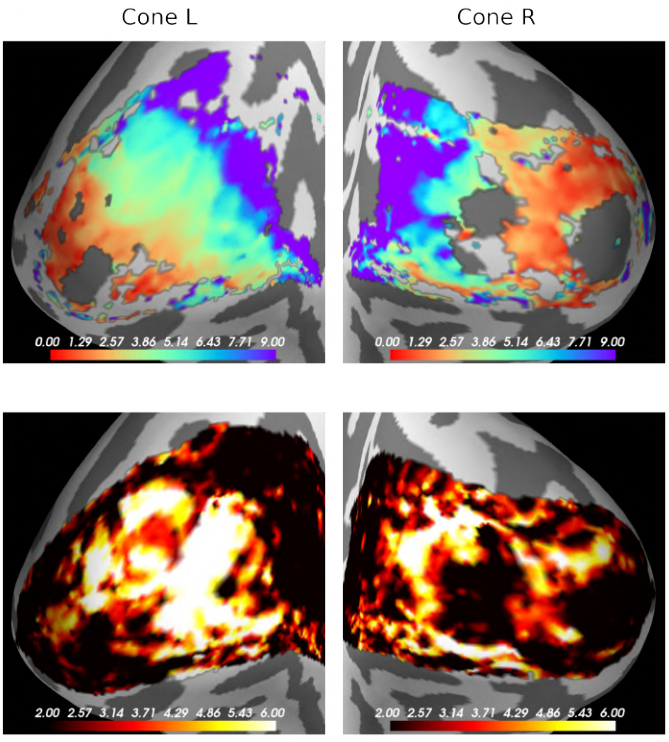

(d) Subject 4

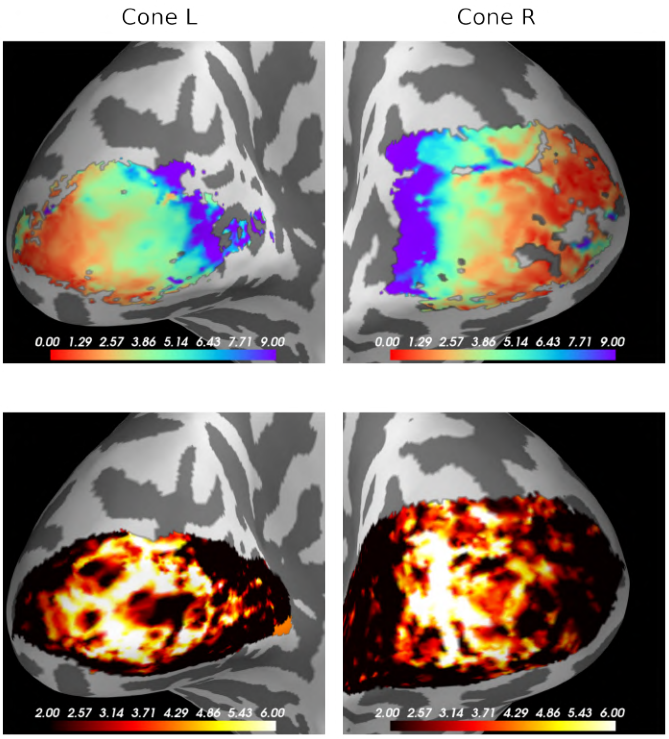

(e) Subject 5

5.2 Study 2

We were interested to know whether the previous results were due to the stimulus itself, the light conditions or a combination of both. In order to test this, we repeated the measurements while inverting the light conditions. Therefore, we used the cone specific stimulus at very-low and low luminance levels and the rod-selective stimulus at high luminance levels.

Low Luminance Levels

The results when using the cone-selective stimulus at low luminance levels are very comparable to those of Study 1 at low illumination. The activation is again limited to the posterior region of V1. When using the ND512 filter (Figure 32, columns one and two) as well as when using the ND256 filter (Figure 32, columns three and four). Figure 32 shows the results for the averaged bar stimulus runs (upper row) as well as those for the full-field stimulus (lower row). The results of using the ND256 filter show activation further towards the posterior part of V1, corresponding with the central region of the visual field. But the main activation remains in the anterior region, corresponding with the peripheral areas of the visual field. The results of the pRF measurements are consistent with those of the full-field stimulus.

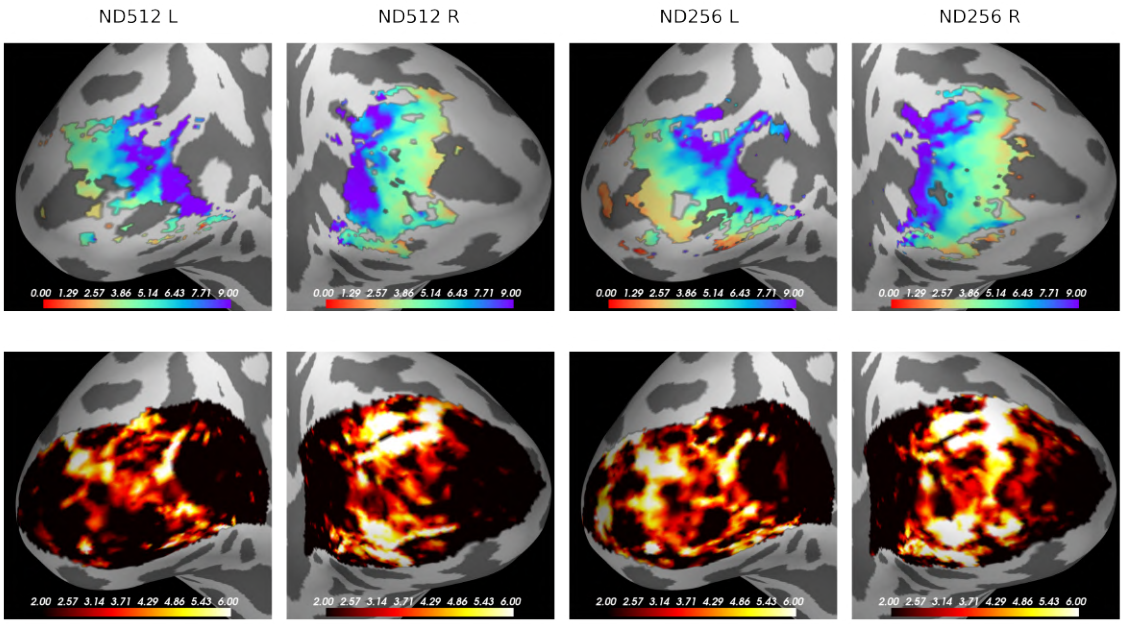

(a) Subject 1

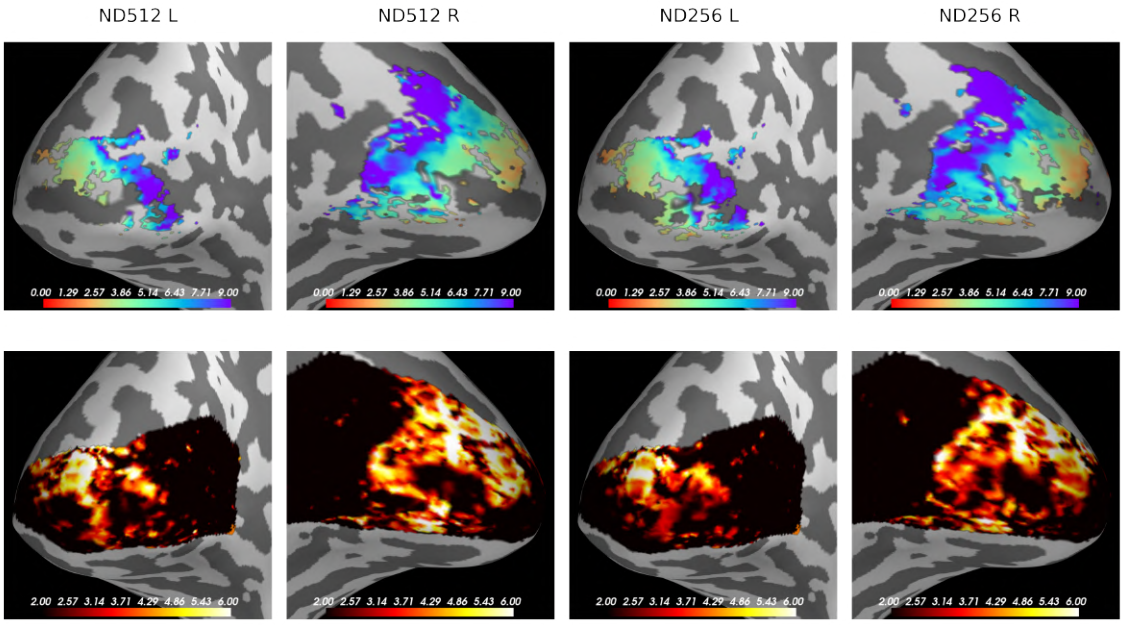

(b) Subject 6

Figure 32: **Results for cone-selective stimulus at low luminance levels**
The results of using the cone-selective stimulus in combination with the ND512 filter are shown in the first two columns. The third and fourth column show the results using the ND256 filter. Study 2 was performed with three subjects (Figure 32a to 32c).
Using a ND256 filter results in a slight increase in activation in the posterior region of V1, compared to using a ND512 filter. But ultimately, the activation remains limited to the anterior region. This indicates the stimulation of predominantly rods.

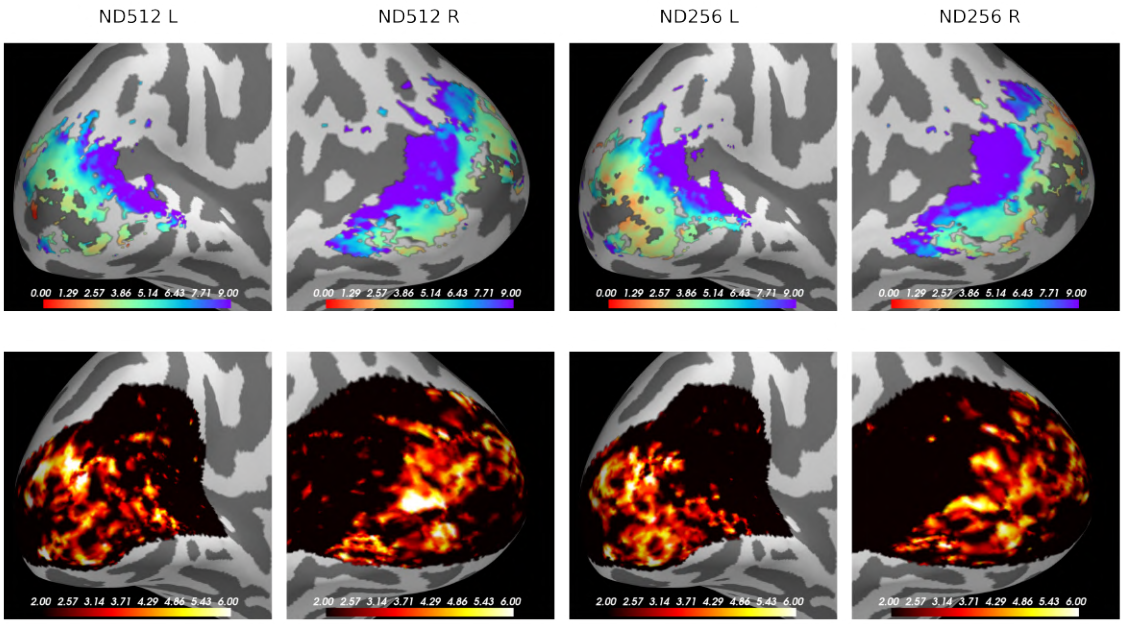

(c) Subject 7

High Luminance Levels

When using the rod-selective stimulus at high luminance levels, all regions of the primary visual cortex are activated (Figure 33). As with the previous figures, the upper images show the results of the averaged pRF runs and the lower images those of the full-field stimulus. While the activation is increased, compared to the cone-selective stimulus at low illumination, across the whole V1, the most noticeable difference can be seen in the posterior region. The activation in the posterior region of V1, corresponding to the central visual field, has increased the most. The results are consistent for both functional tasks as well as all measured subjects (Figure 33a to Figure 33c). The activation in the posterior part of V1 indicates the activation of cones during these measurements.

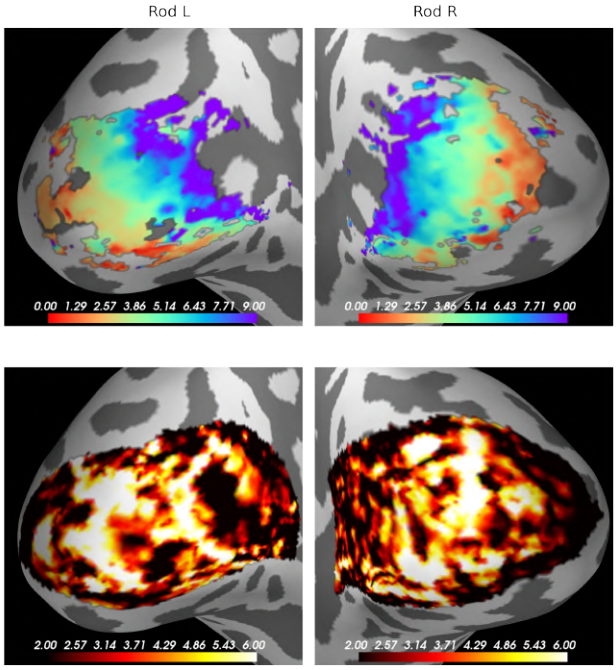

(a) Subject 1

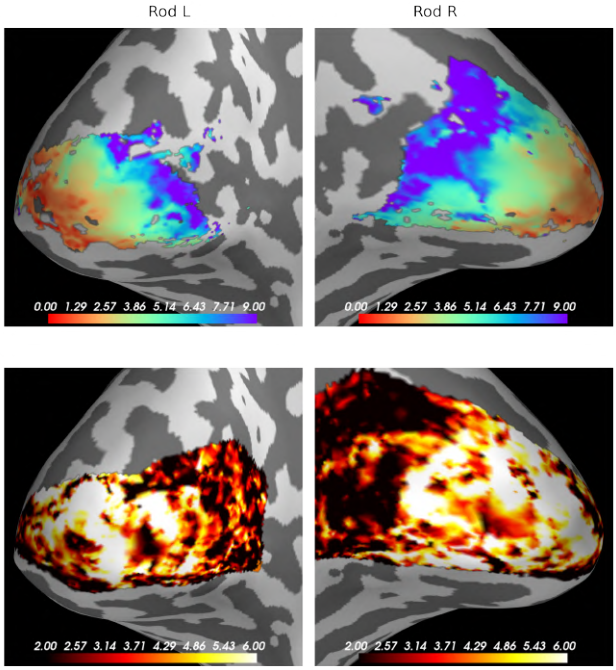

(b) Subject 6

Figure 33: **Results for rod-selective stimulus at high luminance levels** The activation maps of V1 show activation across the entire V1, when using the rod-selective stimulus at full brightness (Figure 33a to 33c). This, particularly the activation in the posterior region, suggests the activation of cones.

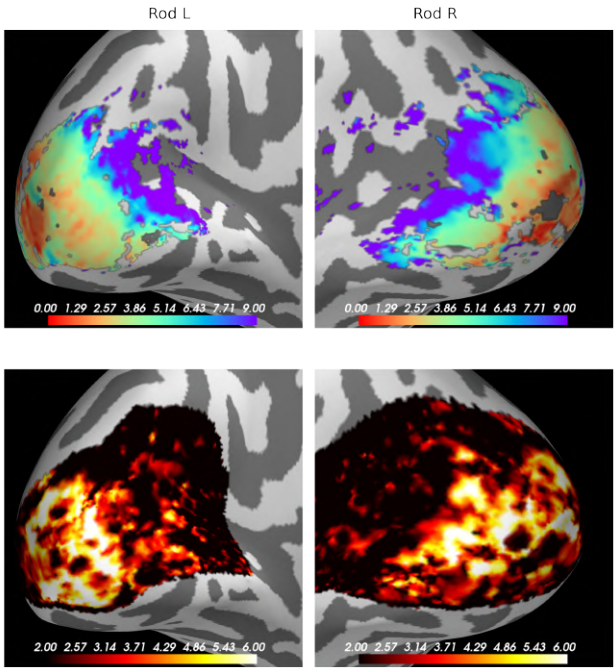

(c) Subject 7

5.3 Distribution of Activated Voxel

In addition to the cortex maps, we were interested in the distribution of the activated voxels over the eccentricity of the visual field. Figure 34 displays the activated voxels per degree of eccentricity for the individual tasks, summed up for all subjects. Figure 34a shows the results for Study 1 and Figure 34b for Study 2. To ensure comparability between the two experiments, the total number of activated voxels has been divided by the number of participants.

For the rod-selective stimulus measured using the ND512 (Figure 34a, blue) or ND256 filter (Figure 34a, orange), it shows very few activated voxels up to 2° field of view. The number of voxels reaches its maximum at around 4°, before it decreases slightly. The low number of activated voxels below 2° aligns with the size of the fovea. Since this region on the retina is devoid of rods, this indicates the activation of predominantly rods during these tasks.
The number of voxels activated during the cone-selective stimulus at full brightness (Figure 34a, green) is substantially higher below 2° field of view. It increases rapidly at around 1° and reaches its maximum around 2° before it decreases. The distribution of the active voxels aligns with the distribution of cones on the retina (Figure 19), further reinforcing the indication that cones are activated during this task.

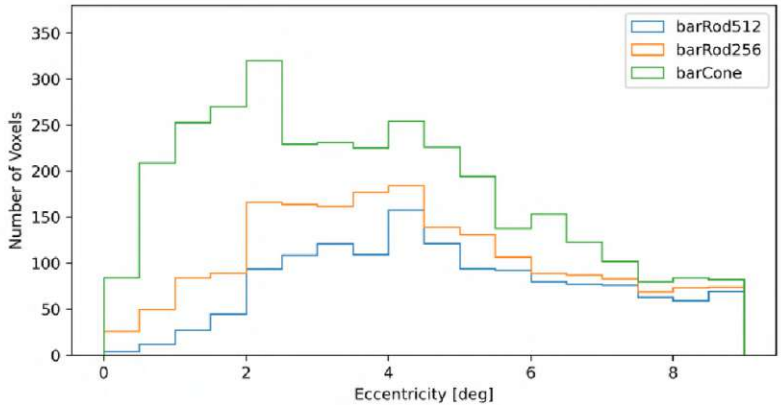

(a) Study 1

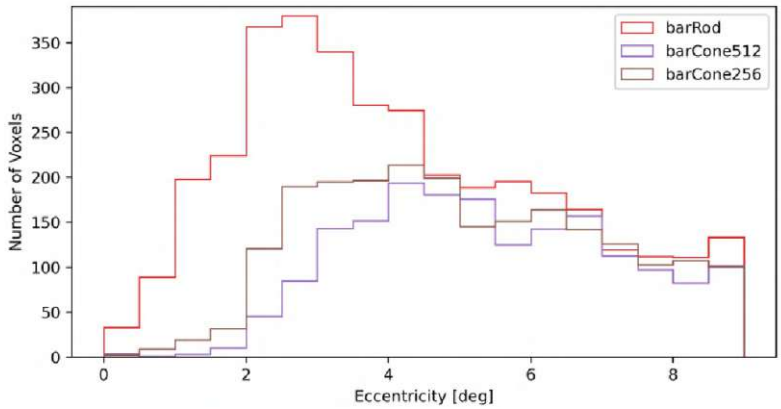

(b) Study 2

Figure 34: **Mean Number of voxels over eccentricity**
These figures show the mean number of activated voxels across all subjects per degree of eccentricity, for all measured tasks. (a) For the rod-selective stimulus at low luminance levels (blue and orange), the number of activated voxels is very low for eccentricities below 2°. This aligns with the size of the fovea, a region on the retina where only cones and no rods are present. This indicates the activation of only rods during these measurements. When using the cone-selective stimulus at high luminance levels (green), the amount of activated voxels is substantially higher below 2°. It reaches its maximum around 2° and then decreases. This aligns with the distribution of cones on the retina. (b) The distribution for the rod-selective stimulus at high luminance (red) is similar to the one for the cone-selective one under the same conditions. This indicates cones being the source of activation. The distribution of the cone-selective stimulus at low luminance levels (purple and brown) on the other hand, matches the distribution of the rod-selective stimulus at these brightness levels. This indicates the activation of predominantly rods during these runs.

The distribution of activated voxels for the rod-selective stimulus at high luminance levels (Figure 34b, red) behaves similar to the one for the cone-selective stimulus. The number of active voxels is slightly lower below 2° than for the cone-selective stimulus, but the shape of curve is very similar. This indicates that during this run predominantly cones were activated.
For the cone-selective stimulus at very low and low luminance levels, using a ND512 (Figure 34b, purple) or ND256 filter (Figure 34b, brown), the number of activated voxels below 2° is even less than for the rod-selective stimulus. The amount increases at the 2° mark, similarly to the rod-selective stimulus under the same conditions. It reaches its maximum around 4° to 5° before it decreases slightly towards the end of the stimulated field at 9°. This distribution likely indicates the activation of rods during these tasks.

5.4 Activation in Fovea

To further compare the results, we took at the look at the specific activation in the fovea. For this we calculated the relative number of above threshold voxels within the foveal 2° compared to the number of all above threshold voxels. This value was calculated for every subject independently and then averaged across subjects. We did this for different variance explained thresholds, between 4% and 20%. The results for all tasks, including the standard error, are shown in Figure 35.

The relative activation in the fovea is highest for the cone-selective stimulus at full brightness. Followed by the rod-selective stimulus at full brightness and low luminance levels (ND256). For the rod-selective stimulus at very low illumination (ND512), the activation in the fovea is quite low. And for the cone-selective stimulus at low luminance levels (ND512 and ND256) practically no activation remains. The curves are mainly flat, with only a slight decrease for higher thresholds. This suggests that the measured effects are stable throughout all thresholds.
This shows that the most photoreceptors were activated during the cone- and rod-selective tasks at full brightness, matching the activation of cones during these tasks. The cone-selective stimulus activates all cone types, resulting in the strongest activation. The rod-selective stimulus, while silencing L- and M- cones, still activates S-cones. Therefore, S-cones contribute to the activation below 2°. The percentage of activation for the rod-selective stimulus at low illumination indicates the activation of rods, even at these low eccentricities.

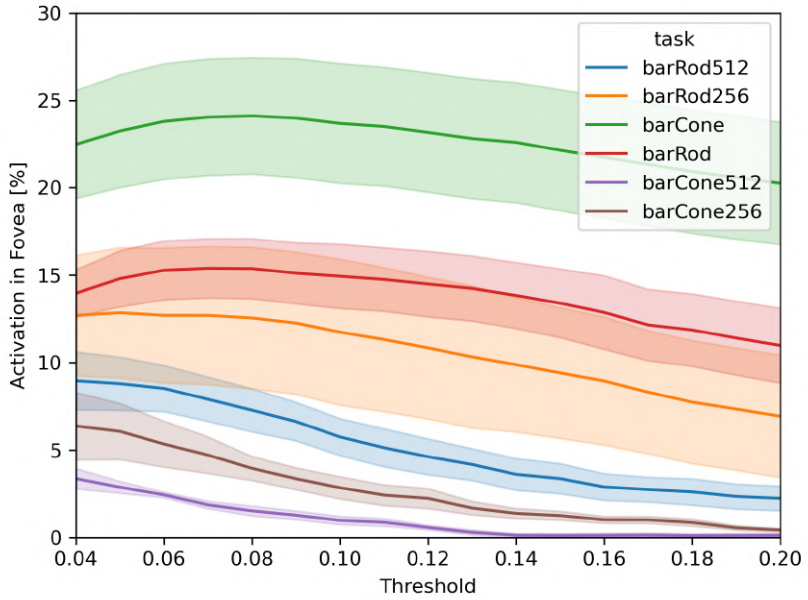

Figure 35: **Activation in the Fovea**

6 Discussion

In this thesis we aim at selectively activating individual retinal photoreceptor subtypes using pRF-mapping stimuli. Stimuli were generated using silent substitution, a method that uses chromatic pairs to activate one photoreceptor subtype while silencing other subtypes. The maximum number of silenced photoreceptors depends on the number of available primary colours [75]. We calculated two colour combinations to generate the stimuli. One stimulus is set to activate mainly rods and one to activate mainly cones (Figure 28). Additionally, the response to the stimuli was measured at different light conditions. For Study 1, five healthy participants were measured. The response to the rod-selective stimulus was recorded at very low and low luminance levels. This ensured scotopic vision, a state where only rods are active, as cones are insensitive to these low levels of light [34]. Optimal sensitivity was achieved by allowing the participants to adapt to the low light conditions for 30 minutes. Two neutral density filters, a ND512 and a ND256, were used during the two rod-selective measurements to adapt the brightness of the projected image. The functional measurements using the cone-selective stimulus were performed without any filters. The resulting brightness levels caused photopic vision. Photopic vision occurs at high illumination levels and is a state were rods are effectively saturated, leaving only cones to be activate [34].
In Study 2, three healthy subjects participated and the light conditions were reversed. The cone-selective stimulus was measured at low luminance levels, with the ND512 and ND256 filter, while the rod-selective stimulus was measured at full brightness. We compared the results of the six respective functional tasks.

6.1 Cone-Selective Stimulus at High Luminance Levels

When using the cone-selective stimulus at high luminance levels the activation maps (Figure 31) show activation on the entire primary visual cortex. The distribution of activated voxels (Figure 34a) further confirms this. While it shows activation over the entire visual field, the number of activated voxels is highest between 1° and 2°, before it decreases for higher eccentricity regions. Additionally, the cone-selective stimulus elicits the highest activation in the foveal area (up to 2°) compared to the total activation (Figure 35). This distribution of activated voxels fits the distribution of the cones on the retina (Figure 19), indicating that cones contribute to the measured activation. The assumption that only cones, an no rods, were activated during this tasks is supported, in addition to the stimulus design, by the illumination conditions. At full brightness, rods are saturated [34], and consequently they do not contribute to the measured activation.
Our ability to selectively activate cones align with the findings of Farahbakhsh et al. [35], who used silent substitution to show that gene therapy can reactivate cone-mediated pathways in children with achromatopsia. They were able to use silent substitution to calculate a cones selective stimulus and successfully generate a cone-mediated pRF map ([35], Supplementary Material). It is important to note, that while our data was recorded on 5 healthy participants, the pRF data of Farahbakhsh et al. was averaged across 28 participants.

6.2 Rod-Selective Stimulus at Low Luminance Levels

For the rod-selective stimulus at very low luminance levels (ND512 and ND256) both functional tasks, using either a bar or a full-field stimulus, yielded very low activation in the posterior part of V1, which corresponds to the central region of the visual field [83]. Whereas the anterior region of V1, corresponding to the peripheral area of the visual field, shows a substantial amount of activation (Figure 30). The activated region aligns with the distribution of rods on the retina (Figure 19), as the amount of rods is higher in the peripheral region of the retina than in the central region [34]. The distribution of activation can also be seen in Figure 34a. When using the ND512 or ND256 filter, the number of activated voxels at eccentricities below 2° is low, but not zero. This is shown as well, when looking the activation in the foveal region compared to the total activation (Figure 35). While the activation is higher when the ND256 filter was used, there is also activation in the foveal region for the ND512 filter. This activation below 2° is most likely due to the activation of rods, as the L- and M-cones were silenced using silent substitution and additionally cone responses are reduced due to low illumination levels. Even though, the fovea contains no rods, this can be explained through multiple reasons. Firstly, while the fovea has a dimension of 2° [34], its central region the umbo, with a diameter <0.5°, is the region that actually contains absolutely no rods [51]. The density of rods in the surrounding fovea is low, however they are present. Secondly, for such central regions the pRF results, pRF size and position, may be too imprecise and the signal may contain contributions from the adjacent area. And even small eye movements may lead to the stimulus activating regions outside the fovea and therefore to imprecise mapping of the foveal region. Due to the low light conditions we were unable to record eye movements using the Eyetracker. We could only use it to manually check

the attentiveness of our participants. Due to these factors limiting the pRF results, we conclude that most likely rod activation contributed to these measurements. These results are in line with Farahbakhsh et al. [35]. They used a rod-selective stimulus, silencing L- and M-cones, at low illumination levels to separate previously existing rod-mediated signals from post-treatment cone-mediated signals. The resulting activation in the visual cortex ([35], Supplementary Materials) matches our areas of activation (Figure 30). Again, while we recorded the data of 5 participants, the rod-mediated pRF map from Farahbakhsh et al. was generates by averaging across 26 participants, making direct comparisons difficult.

6.3 Rod-Selective Stimulus at High Luminance Levels

The rod-selective stimulus at full brightness evokes activation across the entire primary visual cortex (Figure 33), for both functional tasks. Indicating activation of photoreceptors across the entire retina. This can be seen in the distribution of activated cones (Figure 34b) as well. The distribution is similar to the one for the cone-selective stimulus at full brightness (Figure 34a). The number of activated voxels increases until it reaches its maximum between 2° to 3°, before it decreases again. As with the cone-selective stimulus, this distribution matches the distribution of cones on the retina (Figure 19), indicating that this task lead to the activation of cones. Additionally, we can assume that no rods were active, because with such high luminance levels we achieve photopic vision where rods are saturated [34]. Since our setups consists of only three primary colours, the rod-selective stimulus only silences L- and M-cones. Therefore, it is reasonable to assume that the measured response is due to the activation of S-cones. Since the number of S-cones is lower than the number of L- and M-cones [34], this explains also the lower percentage of activation in the fovea compared to the cone-selective stimulus at full brightness (Figure 35).

6.4 Cone-Selective Stimulus at Low Luminance Levels

When using the cone-selective stimulus at low brightness levels, the resulting activation is limited to the anterior regions of V1 (Figure 32), which correspond to the peripheral region of the visual field [34]. This is confirmed by the distribution of activated voxels across the eccentricity of the visual field (Figure 34b). Below 2° almost no voxels are activated, at around 2° the number increases rapidly before decreasing slightly towards the end of the stimulated field. When looking at the activation corresponding to the fovea, compared to the entire visual field, almost no activation takes place (Figure 35). The distribution of activated voxels and the low response in the central field of view indicates the activation of rods. This is further supported by the response of the receptors at these light conditions, as these light levels are too low for cones to be activated [34]. This result indicates that the cone-selective stimulus is not able to silence rods completely. This may be due to errors during the original measurements of the calibration data or due to unknown intrinsic properties of the projector.

7 Conclusion

In the course of this thesis, fMRI measurements were performed on seven healthy subjects on a 3T SIEMENS Prisma Fit scanner. The participants were presented two different stimuli at very-low, low and high illumination respectively, resulting in a total of 6 sets of functional measurements. The aim of this thesis was to selectively activate individual retinal photoreceptor subtypes, i.e. rods and cones. This was done by using silent substitution, a method that uses the photoreceptors inability to distinguish between changes in wavelength and changes in intensity to activate one photoreceptor subtype while keeping the activation constant for the silenced receptors. To achieve this, we calculated two chromatic pairs to generate two different pRF-mapping stimuli: One that selectively activates rods and one that activates cones. In addition to the pRF measurements, a full-field stimulus was measured with the same colour combination. In Study 1, performed on five participants, the rod-selective stimulus was measured at very-low and low luminance levels, achieved by covering all light sources within the scanner room and using a neutral density filter with two different amounts of transmission (ND512 or ND256). Additionally the participants spent 30 minutes in the dark to adapt to the low light conditions. The cone-selective stimulus was measured at high luminance levels. In Study 2, performed on three participants, the stimulus and light conditions were switched. The rod-selective stimulus was measured at full brightness and the cone-selective one at very-low and low luminance levels (ND512 and ND256). The results of the different tasks were displayed in the form of activation maps and as distribution maps of the activated voxels.

The resulting activation maps for the cone-selective stimulus at full brightness show activation across the entire primary visual cortex (V1). And the distribution plot shows the highest number of activated voxels corresponding to the central region of the visual field. This matches with the distribution of cones on the retina and therefore indicates the activation of predominantly cones. This was ensured, in addition to the stimulus design, by the light conditions. At such high illumination levels rods are saturated and therefore, they do not contribute to the measured response.
Similar results were observed for the rod-selective stimulus at full brightness. The activation as well as the distribution is similar to the results for the cone-selective stimulus. The results therefore indicate the activation of cones for this task, especially since rods are saturated. Since the projector that was used is only able to produce three primary colours, only two types of cones could be silenced, L- and M-cones. This leaves the third type of cone receptor, the S-cones, active.
For the rod-selective stimulus at very-low and low luminance levels, the activation is limited to the anterior part of V1, which corresponds to the peripheral region of the visual field. This can be seen at the distribution as well, the number of activated voxels is very low below 2° eccentricity and considerably higher at the periphery of the stimulated field. This distribution aligns with the distribution of rods on the retina. Additionally, the activation of cones was prevented by the low light conditions. Since cones are not yet stimulated at such low levels of light. All this indicates the activation of only rods during these tasks. The result of activated voxels in the foveal region, below 2°, is unexpected as no rods are present at this

area of the retina. But it can be explained by taking a closer look at the fovea and its subsections. The actual region without any rods is only the most central region, below 0.5°. The remaining fovea may contain some rods. Additionally, even small eye movements may influence the pRF mapping accuracy at such small eccentricities. This could lead to voxels of the border region being fitted into the centre of the visual field and therefore explains the presence of activated voxels below 2°.
The cone-selective stimulus at very low and low luminance conditions shows a similar activation and distribution as the rod-selective stimulus under the same conditions. And since cones are not activated at these light levels, these results indicate the activation of rods during this tasks. This suggests that the cone-selective stimulus was not able to fully silence rod activation. This may be due to errors during the measurements of the calibration data or due to some unknown projector properties. This activation of rods can be resolved by using this stimulus at high illumination levels.

In conclusion, this study was able to demonstrate the selective activation of individual photoreceptors. We were able to show that silent substitution is an effective tool to generate pRF mapping stimuli for activating individual photoreceptor subtypes. It is important to note that in addition to the stimulus design it is important to take the measurement conditions into account and to adjust the light levels to the properties of the photoreceptor of interest.

Figures

Tables

References

[1] Alexandre Abraham et al. "Machine learning for neuroimaging with scikit-learn". English. In: *Frontiers in Neuroinformatics* 8 (2014). ISSN: 1662-5196. DOI: 10.3389/fninf.2014.00014. URL: https://www.frontiersin.org/articles/10.3389/fninf.2014.00014/full.

[2] Jesper L.R. Andersson, Stefan Skare, and John Ashburner. "How to correct susceptibility distortions in spin-echo echo-planar images: application to diffusion tensor imaging". In: *NeuroImage* 20.2 (2003), pp. 870–888. ISSN: 1053-8119. DOI: 10.1016/S1053-8119(03)00336-7. URL: https://www.sciencedirect.com/science/article/pii/S1053811903003367.

[3] B.B. Avants et al. "Symmetric diffeomorphic image registration with cross-correlation: Evaluating automated labeling of elderly and neurodegenerative brain". In: *Medical Image Analysis* 12.1 (2008), pp. 26–41. ISSN: 1361-8415. DOI: 10.1016/j.media.2007.06.004. URL: http://www.sciencedirect.com/science/article/pii/S1361841507000606.

[4] Gareth Barker. *MRI: The Classical Description*. URL: https://cds.ismrm.org/protected/16MProceedings/PDFfiles/7101.html. (accessed: 13.05.2025).

[5] Yashar Behzadi et al. "A component based noise correction method (CompCor) for BOLD and perfusion based fMRI". In: *NeuroImage* 37.1 (2007), pp. 90–101. ISSN: 1053-8119. DOI: 10.1016/j.neuroimage.2007.04.042. URL: http://www.sciencedirect.com/science/article/pii/S1053811907003837.

[6] Felix Bloch and WWPM Hansen. "W., Packard, M. The nuclear induction experiment". In: *Physical review* 70.7-8 (1946), pp. 474–485.

[7] Photograph: Danny Hope from Brighton & Hove UK and Diagram: User:Zyxwv99. *File:Macula.svg*. URL: https://commons.wikimedia.org/wiki/File:Macula.svg. License = https://creativecommons.org/licenses/by/2.0/ (accessed: 25.03.2025).

[8] Mark A. Brown and Richard C. Semelka. *MRI: Basic Principles and Applications*. Wiley, Aug. 2003. Chap. 1. ISBN: 9780471467939. DOI: 10.1002/0471467936. URL: http://dx.doi.org/10.1002/0471467936.

[9] Mark A. Brown and Richard C. Semelka. *MRI: Basic Principles and Applications*. Wiley, Aug. 2003. Chap. 2. ISBN: 9780471467939. DOI: 10.1002/0471467936. URL: http://dx.doi.org/10.1002/0471467936.

[10] Mark A. Brown and Richard C. Semelka. *MRI: Basic Principles and Applications*. Wiley, Aug. 2003. Chap. 3. ISBN: 9780471467939. DOI: 10.1002/0471467936. URL: http://dx.doi.org/10.1002/0471467936.

[11] Mark A. Brown and Richard C. Semelka. *MRI: Basic Principles and Applications*. Wiley, Aug. 2003. Chap. 4. ISBN: 9780471467939. DOI: 10.1002/0471467936. URL: http://dx.doi.org/10.1002/0471467936.

[12] Mark A. Brown and Richard C. Semelka. *MRI: Basic Principles and Applications*. Wiley, Aug. 2003. Chap. 5. ISBN: 9780471467939. DOI: 10.1002/0471467936. URL: http://dx.doi.org/10.1002/0471467936.

[13] Mark A. Brown and Richard C. Semelka. *MRI: Basic Principles and Applications*. Wiley, Aug. 2003. Chap. 6. ISBN: 9780471467939. DOI: 10.1002/0471467936. URL: http://dx.doi.org/10.1002/0471467936.

[14] Robert W Brown et al. *Magnetic resonance imaging*. en. Ed. by Robert W Brown et al. 2nd ed. Chichester, England: Wiley-Blackwell, 2014. Chap. 1.

[15] Robert W Brown et al. *Magnetic resonance imaging*. en. Ed. by Robert W Brown et al. 2nd ed. Chichester, England: Wiley-Blackwell, 2014. Chap. 8.

[16] Richard B. Buxton. *Introduction to Functional Magnetic Resonance Imaging: Principles and Techniques*. Cambridge University Press, Aug. 2009. Chap. 14. ISBN: 9780521899956. DOI: 10.1017/cbo9780511605505. URL: http://dx.doi.org/10.1017/CBO9780511605505.

[17] R. Ciric et al. "TemplateFlow: FAIR-sharing of multi-scale, multi-species brain models". In: *Nature Methods* 19 (2022), pp. 1568–1571. DOI: 10.1038/s41592-022-01681-2.

[18] Robert W. Cox and James S. Hyde. "Software tools for analysis and visualization of fMRI data". In: *NMR in Biomedicine* 10.4-5 (1997), pp. 171–178. DOI: 10.1002/(SICI)1099-1492(199706/08)10:4/5<171::AID-NBM453>3.0.CO;2-L.

[19] Anders M. Dale, Bruce Fischl, and Martin I. Sereno. "Cortical Surface-Based Analysis: I. Segmentation and Surface Reconstruction". In: *NeuroImage* 9.2 (1999), pp. 179–194. ISSN: 1053-8119. DOI: 10.1006/nimg.1998.0395. URL: http://www.sciencedirect.com/science/article/pii/S1053811998903950.

[20] Brian M. Dale, Mark A. Brown, and Richard C. Semelka. *MRI Basic Principles and Applications*. Wiley, Aug. 2015. Chap. 1. ISBN: 9781119013068. DOI: 10.1002/9781119013068. URL: http://dx.doi.org/10.1002/9781119013068.

[21] Brian M. Dale, Mark A. Brown, and Richard C. Semelka. *MRI Basic Principles and Applications*. Wiley, Aug. 2015. Chap. 2. ISBN: 9781119013068. DOI: 10.1002/9781119013068. URL: http://dx.doi.org/10.1002/9781119013068.

[22] Brian M. Dale, Mark A. Brown, and Richard C. Semelka. *MRI Basic Principles and Applications*. Wiley, Aug. 2015. Chap. 3. ISBN: 9781119013068. DOI: 10.1002/9781119013068. URL: http://dx.doi.org/10.1002/9781119013068.

[23] Brian M. Dale, Mark A. Brown, and Richard C. Semelka. *MRI Basic Principles and Applications*. Wiley, Aug. 2015. Chap. 4. ISBN: 9781119013068. DOI: 10.1002/9781119013068. URL: http://dx.doi.org/10.1002/9781119013068.

[24] Brian M. Dale, Mark A. Brown, and Richard C. Semelka. *MRI Basic Principles and Applications*. Wiley, Aug. 2015. Chap. 5. ISBN: 9781119013068. DOI: 10.1002/9781119013068. URL: http://dx.doi.org/10.1002/9781119013068.

[25] PM Daniel and D Whitteridge. "The representation of the visual field on the cerebral cortex in monkeys". In: *The Journal of physiology* 159.2 (1961), p. 203.

[26] Garikoitz Lerma-Usabiaga David Linhardt. *dlinhardt/prfprepare*. URL: https://github.com/fmriat/prfprepare?tab=readme-ov-file#readme. (accessed: 19.03.2025).

[27] KO Donner and WAH Rushton. "Retinal stimulation by light substitution". In: *The Journal of physiology* 149.2 (1959), p. 288.

[28] Serge O. Dumoulin and Brian A. Wandell. "Population receptive field estimates in human visual cortex". In: *NeuroImage* 39.2 (2008), pp. 647–660. ISSN: 1053-8119. DOI: https://doi.org/10.1016/j.neuroimage.2007.09.034. URL: https://www.sciencedirect.com/science/article/pii/S1053811907008269.

[29] Allen D. Elster. *BOLD and Brain Activity*. URL: https://mriquestions.com/does-boldbrain-activity.html. (accessed: 19.12.2024).

[30] Allen D. Elster. *k-space*. URL: https://mriquestions.com/what-is-k-space.html. (accessed: 08.04.2025).

[31] Allen D. Elster. *The k-space "grid"*. URL: https://mriquestions.com/k-space-grid.html#/. (accessed: 04.12.2024).

[32] Oscar Esteban et al. "fMRIPrep". In: *Software* (2018). DOI: 10.5281/zenodo.852659.

[33] Oscar Esteban et al. "fMRIPrep: a robust preprocessing pipeline for functional MRI". In: *Nature Methods* 16 (2019), pp. 111–116. DOI: 10.1038/s41592-018-0235-4.

[34] Mark D Fairchild. *Color Appearance Models*. en. 2nd ed. Wiley-IS&T Series in Imaging Science and Technology. Chichester, England: John Wiley & Sons, Nov. 2004.

[35] Mahtab Farahbakhsh et al. "A demonstration of cone function plasticity after gene therapy in achromatopsia". In: *Brain* 145.11 (Aug. 2022), pp. 3803–3815. ISSN: 0006-8950. DOI: 10.1093/brain/awac226. eprint: https://academic.oup.com/brain/article-pdf/145/11/3803/47172197/awac226.pdf. URL: https://doi.org/10.1093/brain/awac226.

[36] Scott H Faro and Feroze B Mohamed. *Functional MRI*. en. Ed. by Scott H Faro and Feroze B Mohamed. 1st ed. New York, NY: Springer, Dec. 2006. Chap. 4.

[37] Scott H Faro and Feroze B Mohamed. *Functional MRI*. en. Ed. by Scott H Faro and Feroze B Mohamed. 1st ed. New York, NY: Springer, Dec. 2006. Chap. 1.

[38] Scott H Faro and Feroze B Mohamed. *Functional MRI*. en. Ed. by Scott H Faro and Feroze B Mohamed. 1st ed. New York, NY: Springer, Dec. 2006. Chap. 2.

[39] VS Fonov et al. "Unbiased nonlinear average age-appropriate brain templates from birth to adulthood". In: *NeuroImage* 47, Supplement 1 (2009), S102. DOI: 10.1016/S1053-8119(09)70884-5.

[40] *Functional Magnetic Resonance Imaging - Advanced Neuroimaging Applications*. InTech, May 2012. Chap. 2. ISBN: 9789535105411. DOI: 10.5772/2512. URL: http://dx.doi.org/10.5772/2512.

[41] *Glossary*. URL: https://nilearn.github.io/dev/glossary.html. (accessed: 19.03.2025).

[42] K. Gorgolewski et al. “Nipype: a flexible, lightweight and extensible neuroimaging data processing framework in Python”. In: *Frontiers in Neuroinformatics* 5 (2011), p. 13. DOI: 10.3389/fninf.2011.00013.

[43] Krzysztof J. Gorgolewski et al. “Nipype”. In: *Software* (2018). DOI: 10.5281/zenodo.596855.

[44] Douglas N Greve and Bruce Fischl. “Accurate and robust brain image alignment using boundary-based registration”. In: *NeuroImage* 48.1 (2009), pp. 63–72. ISSN: 1095-9572. DOI: 10.1016/j.neuroimage.2009.06.060.

[45] *Human photoreceptor distribution.svg*. URL: https://commons.wikimedia.org/wiki/File:Human_photoreceptor_distribution.svg#. accessed: 08.01.2025.

[46] *Intro to GLM Analysis: a single-run, single-subject fMRI dataset*. URL: https://nilearn.github.io/dev/auto_examples/00_tutorials/plot_single_subject_single_run.html. (accessed: 19.03.2025).

[47] Makoto Ishihara. “Versuch einer Deutung der photoelektrischen Schwankungen am Froschauge”. In: *Archiv für die gesamte Physiologie des Menschen und der Tiere* 114.11 (1906), pp. 569–618.

[48] Mark Jenkinson et al. “Improved Optimization for the Robust and Accurate Linear Registration and Motion Correction of Brain Images”. In: *NeuroImage* 17.2 (2002), pp. 825–841. ISSN: 1053-8119. DOI: 10.1006/nimg.2002.1132. URL: http://www.sciencedirect.com/science/article/pii/S1053811902911328.

[49] Muhammad A Kamran, Myung Yung Jeong, and Malik MN Mannan. “Optimal hemodynamic response model for functional near-infrared spectroscopy”. In: *Frontiers in behavioral neuroscience* 9 (2015), p. 151.

[50] Arno Klein et al. “Mindboggling morphometry of human brains”. In: *PLOS Computational Biology* 13.2 (2017), e1005350. ISSN: 1553-7358. DOI: 10.1371/journal.pcbi.1005350. URL: http://journals.plos.org/ploscompbiol/article?id=10.1371/journal.pcbi.1005350.

[51] Helga Kolb et al. *The Architecture of the Human Fovea By Helga Kolb, Ralph Nelson, Peter Ahnelt, Isabel Ortuño-Lizarán and Nicolas Cuenca*. URL: https://webvision.med.utah.edu/book/part-ii-anatomy-and-physiology-of-the-retina/the-architecture-of-the-human-fovea/. (accessed: 25.03.2025).

[52] C. Lanczos. “Evaluation of Noisy Data”. In: *Journal of the Society for Industrial and Applied Mathematics Series B Numerical Analysis* 1.1 (1964), pp. 76–85. ISSN: 0887-459X. DOI: 10.1137/0701007. URL: http://epubs.siam.org/doi/10.1137/0701007.

[53] Paul C Lauterbur. “Image formation by induced local interactions: examples employing nuclear magnetic resonance”. In: *nature* 242.5394 (1973), pp. 190–191.

[54] Garikoitz Lerma-Usabiaga et al. “A validation framework for neuroimaging software: The case of population receptive fields”. In: *PLoS computational biology* 16.6 (2020), e1007924.

[55] Zhi-Pei Liang and Paul C Lauterbur. *Principles of magnetic resonance imaging : a signal processing perspective*. eng. IEEE Press series in biomedical engineering. SPIE Optical Engineering Pr., 2000. Chap. 3. ISBN: 0470545658.

[56] David Linhardt. "Stimulus selection in functional magnetic resonance imaging based retinotopic mapping". MA thesis. Wien: Technische Universität Wien, 2020. DOI: 10.34726/hss.2020.65922.

[57] David Linhardt et al. "Combining stimulus types for improved coverage in population receptive field mapping". In: *NeuroImage* 238 (2021), p. 118240.

[58] Mads00. *Neural pathway diagram.svg*. URL: https://commons.wikimedia.org/wiki/File:Neural_pathway_diagram.svg#. accessed: 09.01.2025.

[59] Peter Mansfield. "Multi-planar image formation using NMR spin echoes". In: *Journal of Physics C: Solid State Physics* 10.3 (1977), p. L55.

[60] Peter Mansfield and Peter K Grannell. "NMR'diffraction'in solids?" In: *Journal of Physics C: solid state physics* 6.22 (1973), p. L422.

[61] Joel T Martin et al. "PySilSub: An open-source Python toolbox for implementing the method of silent substitution in vision and nonvisual photoreception research". In: *Journal of Vision* 23.7 (2023), pp. 10–10.

[62] Vladimír Mlynárik. "Introduction to nuclear magnetic resonance". In: *Analytical Biochemistry* 529 (2017). Introduction to in vivo Magnetic Resonance Spectroscopy (MRS): A method to non-invasively study metabolism, pp. 4–9. ISSN: 0003-2697. DOI: https://doi.org/10.1016/j.ab.2016.05.006. URL: https://www.sciencedirect.com/science/article/pii/S0003269716300719.

[63] Steen Moeller et al. "Multiband multislice GE-EPI at 7 tesla, with 16-fold acceleration using partial parallel imaging with application to high spatial and temporal whole-brain fMRI". In: *Magnetic resonance in medicine* 63.5 (2010), pp. 1144–1153.

[64] Seiji Ogawa et al. "Brain magnetic resonance imaging with contrast dependent on blood oxygenation." In: *proceedings of the National Academy of Sciences* 87.24 (1990), pp. 9868–9872.

[65] RJ Ordidge et al. "Real time movie images by NMR". In: *The British journal of radiology* 55.658 (1982), pp. 729–733.

[66] Rémi Patriat, Richard C. Reynolds, and Rasmus M. Birn. "An improved model of motion-related signal changes in fMRI". In: *NeuroImage* 144, Part A (Jan. 2017), pp. 74–82. ISSN: 1053-8119. DOI: 10.1016/j.neuroimage.2016.08.051. URL: http://www.sciencedirect.com/science/article/pii/S1053811916304360 (visited on 01/18/2017).

[67] Jonathan D. Power et al. "Methods to detect, characterize, and remove motion artifact in resting state fMRI". In: *NeuroImage* 84.Supplement C (2014), pp. 320–341. ISSN: 1053-8119. DOI: 10.1016/j.neuroimage.2013.08.048. URL: http://www.sciencedirect.com/science/article/pii/S1053811913009117.

[68] Edward M Purcell, Henry Cutler Torrey, and Robert V Pound. "Resonance absorption by nuclear magnetic moments in a solid". In: *Physical review* 69.1-2 (1946), p. 37.

[69] I. I. Rabi et al. "A New Method of Measuring Nuclear Magnetic Moment". In: *Phys. Rev.* 53 (4 Feb. 1938), pp. 318–318. DOI: 10.1103/PhysRev.53.318. URL: https://link.aps.org/doi/10.1103/PhysRev.53.318.

[70] Lee Ann Remington. *Clinical anatomy and physiology of the visual system*. eng. 3rd ed. Saint Louis, Mo.: Elsevier/Butterworth/Heinemann, 2012. Chap. 4. ISBN: 1455727776.

[71] Charles Smart Roy and Charles S Sherrington. "On the regulation of the blood-supply of the brain". In: *The Journal of physiology* 11.1-2 (1890), p. 85.

[72] R Rzedzian et al. "Real-time nuclear magnetic resonance clinical imaging in paediatrics". In: *The Lancet* 322.8362 (1983), pp. 1281–1282.

[73] Theodore D. Satterthwaite et al. "An improved framework for confound regression and filtering for control of motion artifact in the preprocessing of resting-state functional connectivity data". In: *NeuroImage* 64.1 (2013), pp. 240–256. ISSN: 10538119. DOI: 10.1016/j.neuroimage.2012.08.052. URL: http://linkinghub.elsevier.com/retrieve/pii/S1053811912008609.

[74] Franz Schmitt, Michael K Stehling, and Robert Turner. *Echo-planar imaging: theory, technique and application*. Springer Science & Business Media, 2012. Chap. 1. URL: https://books.google.at/books?hl=de&lr=&id=p10yBwAAQBAJ&oi=fnd&pg=PP16&dq=principles+echo+planar+imaging&ots=-LKSSHpS3g&sig=VlFgQC3UgFVxbnLN3DPRsBhHrkA&redir_esc=y#v=onepage&q&f=false.

[75] Manuel Spitschan and Tom Woelders. "The Method of Silent Substitution for Examining Melanopsin Contributions to Pupil Control". In: *Frontiers in Neurology* 9 (2018). ISSN: 1664-2295. DOI: 10.3389/fneur.2018.00941. URL: https://www.frontiersin.org/journals/neurology/articles/10.3389/fneur.2018.00941.

[76] Blausen.com staff. *Blausen 0103 Brain Sensory Motor.png*. URL: https://commons.wikimedia.org/wiki/File:Blausen_0103_Brain_Sensory%26Motor.png. accessed: 09.01.2025.

[77] Blausen.com staff. *Blausen 0111 BrainLobes.png*. URL: https://commons.wikimedia.org/wiki/File:Blausen_0111_BrainLobes.png. accessed: 09.01.2025.

[78] Blausen.com staff. *Eye Anatomy*. URL: https://commons.wikimedia.org/wiki/File:Blausen_0389_EyeAnatomy_02.png#. accessed: 08.01.2025.

[79] Christoph Stippich, ed. *Clinical functional MRI*. en. Medical Radiology / Diagnostic Imaging. Berlin, Germany: Springer, Mar. 2007. Chap. 1.

[80] Christoph Stippich, ed. *Clinical functional MRI*. en. Medical Radiology / Diagnostic Imaging. Berlin, Germany: Springer, Mar. 2007. Chap. 2.

[81] N. J. Tustison et al. "N4ITK: Improved N3 Bias Correction". In: *IEEE Transactions on Medical Imaging* 29.6 (2010), pp. 1310–1320. ISSN: 0278-0062. DOI: 10.1109/TMI.2010.2046908.

[82] Brian A Wandell. *Foundations of vision.* Sinauer Associates, 1995. Chap. 6.

[83] Brian A. Wandell, Serge O. Dumoulin, and Alyssa A. Brewer. "Visual Field Maps in Human Cortex". In: *Neuron* 56.2 (Oct. 2007), pp. 366–383. ISSN: 0896-6273. DOI: 10.1016/j.neuron.2007.10.012. URL: http://dx.doi.org/10.1016/j.neuron.2007.10.012.

[84] Yikrazuul. *Heme b.svg.* URL: https://commons.wikimedia.org/wiki/File:Heme_b.svg. (accessed: 17.12.2024).

[85] Alicja Zelazko. *RGB colour model.* URL: https://www.britannica.com/science/RGB-color-model. (accessed: 16.03.2025).

[86] Y. Zhang, M. Brady, and S. Smith. "Segmentation of brain MR images through a hidden Markov random field model and the expectation-maximization algorithm". In: *IEEE Transactions on Medical Imaging* 20.1 (2001), pp. 45–57. ISSN: 0278-0062. DOI: 10.1109/42.906424.